Enantiomorphing Chiral Plasmonic Nanostructures: A Counterintuitive Sign Reversal of the Nonlinear Circular Dichroism

Peer-reviewed author version

Collins, Joel T.; Zheng, Xuezhi; Braz, Nuno V. S.; SLENDERS, Eli; Zu, Shuai; Vandenbosch, Guy A. E.; Moshchalkov, Victor V.; Fang, Zheyu; AMELOOT, Marcel; Warburton, Paul A. & Valev, Ventsislav K. (2018) Enantiomorphing Chiral Plasmonic Nanostructures: A Counterintuitive Sign Reversal of the Nonlinear Circular Dichroism. In: ADVANCED OPTICAL MATERIALS, 6(14) (Art N° 1800153).

DOI: 10.1002/adom.201800153
Handle: http://hdl.handle.net/1942/28053

Enantiomorphing chiral plasmonic nanostructures: a counter-intuitive sign reversal of the nonlinear circular dichroism

Joel T. Collins[1], Xuezhi Zheng[2], Nuno V. S. Braz[3,4], Eli Slenders[5], Shuai Zu[6], Guy A. E. Vandenbosch[2], Victor V. Moshchalkov[7], Zheyu Fang[6], Marcel Ameloot[5], Paul A. Warburton[3,4], Ventsislav K. Valev[1*]*

[1] Centre for Photonics and Photonic Materials, and Centre for Nanoscience and Nanotechnology, Department of Physics, University of Bath, Bath, UK

[2] ESAT-TELEMIC, KU Leuven B-3001, Leuven, Belgium

[3] Electrical Engineering, University College London, Torrington Place, London WC1E 7JE, UK

[4] London Centre for Nanotechnology, University College London, 17-19 Gordon St, London, WC1H 0AH, UK

[5] University Hasselt and transnational University Limburg, BIOMED, Diepenbeek, Belgium

[6] School of Physics, State Key Lab for Mesoscopic Physics, and Collaborative Innovation Center of Quantum Matter, Peking University, Beijing 100871, China

[7] Laboratory of Solid State Physics and Magnetism, KU Leuven, Celestijnenlaan 200D, Heverlee, B-3001, Belgium

KEYWORDS

Plasmonic, chirality, nonlinear optics, metamaterials, chiroptical effects

Abstract:
Plasmonic nanostructures have demonstrated a remarkable ability to control light in ways never observed in nature, as the optical response is closely linked to their flexible geometric design. Due to lack of mirror symmetry, chiral nanostructures allow twisted electric field “hotspots” to form at the material surface. These hotspots depend strongly on the optical wavelength and nanostructure geometry. Understanding the properties of these chiral hotspots is crucial for their applications; for instance, in enhancing the optical interactions with chiral molecules. Here, we present the results of an elegant experiment: by designing 35 intermediate geometries, we “enantiomorph” the structure from one handedness to the other, passing through an achiral geometry. We use nonlinear multi-photon microscopy to demonstrate a new kind of double-bisignate circular dichroism due to enantiomorphing, rather than wavelength change. From group theory, we propose a fundamental origin of this plasmonic chiroptical response. Our analysis allows the optimization of plasmonic chiroptical materials.

Throughout the 19th and most of the 20th century, chirality has been associated with chemistry. However, whereas chirality can be crucial for understanding molecules, molecules are not best suited for understanding chirality. Indeed, there are various forms of chirality, such as helical chirality, propeller chirality, supramolecular chirality, extrinsic chirality, etc.[1,2] These forms all depend on intrinsic chirality parameters. Ideally, we would like to be able to vary these parameters, i.e. to follow the parameter values as chiral systems transition from one chiral form into another. However, it is impossible to control the size of atoms, the length of chemical bonds and the orientation of orbitals. Modern nanofabrication techniques have lifted these limitations.

Using modern nanofabrication methods, it is possible to explore the evolution of chiral forms, by preparing numerous intermediate geometries. This is important because it opens the possibility to tune and optimize the chirality parameters, which enable interesting properties. For instance, by maximizing the *geometric chirality* parameter, it is possible to achieve negative refractive index materials.[3] Such materials could lead to super-lenses[4] and various applications that depend on the control of circularly polarized light. In turn, circularly polarized light could find applications in spintronics[5] and quantum computing[6,7]. Moreover, by optimizing a parameter called *optical chirality*[8] it has been shown that "superchiral" light configurations can be achieved. In such configurations, the pitch of the electric field of light is shorter than that of circularly polarized light, thereby enabling stronger chiroptical effects.[9–11] These effects are leading to more sensitive optical detection and characterization of chiral molecules – crucial for the pharmaceutical and chemical industries.[11–13] Importantly, optical chirality is particularly enhanced at the surface of chiral plasmonic nanostructures,[14,15] resulting in large enhancements in measurable circular dichroism (CD).[16–19]

Despite the advantages of creating intermediate geometries, it is rare to find studies where these have been investigated in detail. Between two enantiomorphs, there can be several pathways for intermediate geometries and those might be quite different (**Figure 1a**). Also, a priory, it is not clear what the best number of intermediate geometries should be. In the literature, examples can be found of studying both enantiomorphs of a structure, its achiral variant and a small number of intermediate steps only.[20] Consequently, important interesting behavior can go unnoticed.

Here, we report an elegant experiment, impossible to perform with chiral molecules: by designing 35 intermediate geometries, we "enantiomorph" plasmonic nanostructures from one handedness to the other, passing through an achiral geometry. We demonstrate a new kind of bisignate (of two signs) circular dichroism due to enantiomorphing, rather than wavelength change, in the nonlinear emission from near-field hotspots. Contrary to what would be expected from pure geometric considerations, the nonlinear chiroptical signal reverses sign trice, i.e. it is double-bisignate. In order to understand this result, we perform a full modal analysis of the structures in combination with irreducible representations (group theory). Interestingly, we find that, regardless of their handedness, chiral nanostructures contain modes that can be excited by both left and right circularly polarized light (LCP and RCP). Furthermore, which modes are dominant (i.e. couple strongest to light) depends on the wavelength or the shape/dimensions of the nanostructure. It is therefore perfectly possible to engineer chiral nanomaterials that, at a given wavelength, can only be excited with the "wrong" kind of circularly-polarized light (CPL). Our findings offer the possibility of tuning chiroptical response by selecting particular electromagnetic modes, or sets of modes, among hundreds available, which can enable much more sensitive chiroptical control than what is currently available.

Results|

We begin by presenting the purely geometric considerations. Starting with left-handed crosses, we morph their geometry in discrete steps, first into achiral squares and then into right-handed chiral crosses **(Figure 1b)**. For the purposes of comparison, we use a measure of "chiral geometric difference" to quantify the geometric chirality. This quantity is defined as $1-A_{Overlap}/A_{Total}$, where $A_{Overlap}$ is the area of maximal overlap that can be achieved between left- and right-handed shapes, and A_{Total} is the sum of the areas of the left and right-handed shapes. $A_{Overlap}$ is found by rotating and translating the two mirror-image shapes relative to each other and calculating the maximum overlap. As Figure 1b shows, the chiral geometric difference diminishes until it reaches 0 (in the achiral case) and then reverses sign for the mirrored shapes. This measure of chirality is in stark contrast to the double-bisignate response found in our nonlinear CD measurements.

For our experiments, we made use of multi-photon microscopy performed with CPL illumination at 800 nm and schematized in **Figure 1c**. The instrument was a standard commercial model (the same as in our previous works[21]), with one difference: the collected light was not limited to the second harmonic generation (SHG) but also contained two-photon luminescence (TPL). Both these nonlinear optical processes are enhanced in the regions of strong local field,[22,23] and therefore act as a sensitive probe for local field effects. They can in principle be very different (as SHG is governed by symmetry-selection rules) but here we found that the SHG and the TPL responses were identical (see **Supplementary Figure 1**). Consequently, collecting both increases the detected signal from the samples and allows the use of lower laser power, reducing the risk of potential damage to the samples[24].

The samples are chiral crosses made of Au, deposited by electron beam lithography (EBL) on a Si substrate with a thermal oxide layer, and whose dimensions and depth profile are given in **Figure 1d.** Each cross is composed of four separate nanostripes, with varying width *w* and length *l*. The separation distance between nanostripes, at the centre of the crosses, is constant at 200 nm. The crosses are arranged in a 40×40 μm^2 square array, with the distance between cross centres also kept constant at 3.2 μm.

Figure 2a shows scanning electron microscopy (SEM) images of sample arrays. In these arrays, the length of the nanostripes is fixed (1000 nm) and the width changes from 200 nm to 1000 nm in steps of 200 nm. Underneath each SEM are two corresponding multi-photon micrographs, obtained with LCP and RCP. The multi-photon microscopy images are color-coded for intensity and they show bright hotspots at the center of the chiral crosses (indicated with dashed-line squares for clarity). Similar hotspots have previously been observed at the center of G-shaped[25] and S-shaped[26] nanostructured arrays. The hotspots correspond to a chiral coupling at the center of the unit cells that depends on the chirality of the nanostructures and the direction of CPL[26–28]. This dependence is expressed as a directly observable nonlinear CD effect (brightness of the hotspots, depending on the direction of CPL). Interestingly though, in this set of samples, the nonlinear CD changes sign between the chiral crosses with nanostripe width 200 nm and 600 nm, even though the structures have the same geometric chirality.

The CD reversal can be seen more quantitatively in **Figure 2b**. Here, the nonlinear CD is obtained from the detected light upon LCR or RCP illumination according to $\left(I_{RCP}^{MP} - I_{LCP}^{MP}\right) \Big/ \left(I_{RCP}^{MP} + I_{LCP}^{MP}\right)$. The individual multi-photon intensity terms I_{LCP}^{MP} and I_{RCP}^{MP} were obtained from the pixel intensity at the center of the chiral crosses, where the chiral coupling is maximum and the characteristic response is most pronounced. For each chiral cross, the central

hotspot intensity was averaged over 25 pixels (5×5 pixel array at 0.09 μm per pixel). To account for individual variation between crosses, I_{LCP}^{MP} and I_{RCP}^{MP} were each obtained from further averaging the hotspots of 25 individual crosses. The error bars in **Figure 2b** correspond to the standard deviation from this averaging. It should also be noted that the SEM pictures in **Figure 2a** are only a subset of the entire range of samples we studied. The full set started from *w*=100 nm and progressed to *w*=1000 nm, in steps of 50 nm. Upon considering the nonlinear CD from all these samples, it is obvious that around *w*=200 nm and around *w*=800 nm, the chiroptical response is unambiguously reversed, i.e. with clearly separated error bars. Conversely, in linear scattering spectroscopy measurements **(Supplementary Figure 2**) no significant CD was found. Simulations show that this is unsurprising, as the CD in linear scattering cross sections is found to be to the order of 10^{-4}. Furthermore, FDTD simulations of the linear CD response, in reflection geometry, showed a significantly different behavior than the one in Figure 2b **(Supplementary Figure 3)**. This too is unsurprising as the linear CD measures far-field behavior, which differs from the near-field properties probed by multiphoton spectroscopy.

To understand the reversal of the CD, we need to rigorously examine the electromagnetic behavior at the surface of the nanostructures. Here, we formulate the linear optical light interaction with the structures in the framework of the electric field - volume integral equations (EF-VIEs) [29–34]. For the sake of conciseness, we summarize the electric field volume integral equation in an operator form (for full forms see **Supplementary Discussion 1**),

$$Z(\mathbf{r},\mathbf{r}';\omega)\cdot\mathbf{J}(\mathbf{r}',\omega)=\mathbf{E}_{\mathbf{inc}}(\mathbf{r},\omega), \qquad (1)$$

where $\mathbf{J}(\boldsymbol{r}',\omega)$ represents the full solution, i.e. the induced current (and charge) flowing in a nanostructure due to an incident field $\boldsymbol{E_{inc}}(\boldsymbol{r},\omega)$**,** while the impedance operator $\mathbf{Z}(\boldsymbol{r},\boldsymbol{r}';\omega)$ is related with the Green's function that describes how a part of the nanostructure (at a source point $\mathbf{r}'$)

electromagnetically interacts with another part (at an observation point $\mathbf{r}$). The full solution is characterized by a set of modes that originate from the eigenvalue problem for equation (1) [35]:

$$Z(\mathbf{r},\mathbf{r}';\omega)\cdot\mathbf{J_n}(\mathbf{r}',\omega)=\lambda_n(\omega)\cdot\mathbf{J_n}(\mathbf{r}',\omega), \qquad (2)$$

where each mode $\boldsymbol{J_n}(\boldsymbol{r}',\omega)$ is a complex spatial distribution that is independent of the incident field, at a frequency ω and with a corresponding eigenvalue λ_n.

The EF-VIEs approach is well established but here we take the theoretical analysis a significant step further by making use of group theory. From the discussion detailed in **Supplementary Discussion 2 and 3,**[36] each available mode associated with a given structure geometry can be placed in one of four orthogonal irreducible representations $\Gamma_{j=1,2,3,4}$. These representations correspond to exclusive excitation with either the two orthogonal linear polarizations (Γ_1 for horizontal and Γ_2 for vertical) or the two circular polarizations (Γ_3 for LCP and Γ_4 for RCP). Importantly, each mode in the 3rd irreducible representation has a "correlated" mode in the 4th irreducible representation, with identical eigenvalues forming an "accidentally degenerate pair". Crucially, the LCP coupling coefficient of a given Γ_3 mode may be different from the RCP coupling coefficient of the correlated Γ_4 mode. This difference in a mode pair's ability to couple to LCP and RCP incident light can be seen as a type of "modal circular-dichroism", and is shown in **Figure 3a,b.**

Figure 3a shows pairs of correlated modes in the structures with width 200 nm. In blue, the Γ_3 modes are ranked according to their coupling coefficient to LCP. The correlated Γ_4 modes are shown in red, please note these only couple to RCP. In an achiral structure, both the blue and red sets would have identical values and ranking. Not surprisingly, the presence of chirality in the structure breaks the symmetry and, overall, the blue modes have higher coupling

coefficients. But very counter-intuitively, we also find that, in some pairs, the red modes have higher coupling coefficients. This means that, for such modes, light of the "wrong chirality" couples more efficiently to the chirality of the nanostructure. An example of this behavior is indicated with an arrow on the figure. As we will see next, the exception can become the rule as we continue changing the cross width towards an achiral structure.

Figure 3b shows pairs of correlated modes in the structures with width 800 nm. Here, there are more red-dominant pairs of correlated modes than in **Figure 3a,** to the point that the overall calculated CD is reversed, as in the experimental observation. Therefore, in these plasmonic nanostructures, the chiroptical response originates from the superposition of all the individual modal responses. The modes themselves represent complex spatial distributions of the charge density; as an illustration, the first and second modes from **Figure 3a** and **3b** are shown in **Figure 3c** and **3d** respectively.

Mathematically, the overall CD originates from the full solution obtained by linearly superposing the contributions from all eigenmodes $\boldsymbol{J_n}$,

$$\mathbf{J}(\mathbf{r}',\omega) = \sum c_n(\omega)\mathbf{J_n}(\mathbf{r}',\omega), \tag{3}$$

where, for a given incident field, the coupling coefficients c_n are given by

$$c_n(\omega) = \frac{\int_V \mathbf{J_n}(\mathbf{r}',\omega)\cdot\mathbf{E_{inc}}(\mathbf{r}',\omega)\,d\mathbf{r}'}{\lambda_n(\omega)} \tag{4}$$

and the volume integration is carried out over the whole nanostructure. Full solutions are shown in **Supplementary Figure 4**. To calculate an overall CD, we make use of the inner product of the coupling coefficients given by

$$\left\|c_n(\omega)\right\|^2 = \left\langle c_n(\omega), c_n(\omega)\right\rangle = \sum_n c_n(\omega)c_n^*(\omega). \tag{5}$$

Here, $c_n^*(\omega)$ denotes the complex conjugate of $c_n(\omega)$. Since the local field intensity is dependent on the square of all coupling coefficients, the local field circular-dichroism can be expressed as:

$$\mathrm{CD}^{(Local)} \propto \frac{\left\|c_n{}^R(\omega)\right\|^2 - \left\|c_n{}^L(\omega)\right\|^2}{\left\|c_n{}^R(\omega)\right\|^2 + \left\|c_n{}^L(\omega)\right\|^2}. \qquad (6)$$

The *L* and *R* superscripts refer to the solutions for LCP and RCP (the achiral case of *w*=1000 nm is treated separately, see **Supplementary Discussion 4**). The results from equation (6) can be found in **Figure 3e;** where the calculated CD is plotted as a function of the nanostripe width (*w*), for the left-handed and right-handed crosses. These numerical results show a bisignate CD response corresponding well to the experimental CD curves in **Figure 2b.**

We further verify this agreement with a second set of intermediate structures (**Supplementary Figure 5**) in which the nanostripe length is varied, for a constant width of 200 nm. We observe in both experiments and simulations that the CD emerges away from the achiral structure, and subsequently plateaus. Although longer nanostripes support more electromagnetic modes than shorter ones, the effect of additional modes on the key central region decreases, the longer the nanostripe length. Since the nonlinear CD measurements probe the coupling in the center of the crosses, the effect of increasing nanostripe length on the CD plateaus.

Discussion

This study has focussed on the bisignate CD response as a function of varying structure geometry. With respect to wavelength, both linear and nonlinear chiroptical spectra often exhibit complex bisignate (of two signs) features.[37–41] This behavior can be linked to Kuhn's sum-rule,[42] which states that the chiroptical response must be zero over all wavelengths. This dependence on wavelength has been analyzed in terms of exciton coupling,[43] nanoparticle-nanoparticle

Coulomb coupling,[44] and energy level hybridization.[45] In particular, in the linear optical case it was shown that the energetic ordering of the hybridized modes can be changed, resulting in a reversal of the CD, upon making small relative position shifts between L-shaped nanoparticles.[46]

In this work, we made use of nonlinear chiroptical methods. There are several techniques for mapping near-fields that are based on, for instance, using a superlens,[47,48] a nanorod array,[49] or hotspot decorations.[24] Yet the most popular method of sub-wavelength imaging remains scanning near-field optical microscopy (SNOM),[50] which can be performed with circularly polarized light for studies of chirality.[51–56] For all its advantages, SNOM necessitates long scanning times, which renders impractical the imaging of large areas and large sample arrays. Moreover, SNOM is limited to samples where the near-field is accessible to the tip of the microscope and the presence of the tip itself leads to an increase in complexity.[57] An interesting alternative can therefore be found in nonlinear microscopy. In particular, second harmonic generation (SHG) microscopy is highly sensitive to the near-field intensity, it can probe buried interfaces and, for samples that do not require very high mapping resolution (such as ours), it is fast and practical. Owing to the lack of background, SHG chiroptical techniques are usually three orders of magnitude more sensitive to chirality than their linear optical counterparts,[26–28] which justifies their use.

To summarize, we have shown that the origin of the chiroptical response in plasmonic nanostructures is due to the selective excitation of available modes, therefore any physical property that affects the modes will allow tuning of the chiroptical response. This mechanism could also be used to explain previous experimental observations of bisignate CD spectra, where different sets of modes can be coupled differently depending on the wavelength of light. Furthermore, we can predict that variation of temperature of the nanostructures (e.g. by laser

heating) will change the sets of available modes, due to thermal expansion or a change in permittivity[58], and can lead to tuning the chiroptical response. Further physical processes that involve excitation of specific plasmonic modes (Fano resonance, spasers, electromagnetically induced transparency, etc.) can also be used to tune that response for desired applications (through achieving large chirality parameter). In practice, maximizing the chiroptical response in any plasmonic nanostructure is allowed by suppression of the modes that couple to light “with the wrong chirality”. Equally important, by locally enhancing a particularly strong mode (e.g. via coupling to an auxiliary structure) it is possible to enhance the chiroptical interaction with molecules improving enantioselectivity for molecular sensing, separation and synthesis.

Methods

Sample preparation

Samples were fabricated using an off-the-shelf Silicon wafer with a 100nm thermal oxide layer. A dicing saw was used to slice the wafer into 7.5x7.5 mm^2 samples, followed by a solvent clean and an O_2 plasma ashing step. The samples were spin coated with a 100 nm thick polymethyl methacrylate (PMMA) supplied by MicroChem and formulated with a 950k molecular weight. A sputter coater was used to deposit a 5 nm gold layer on top of the PMMA, which helped minimize charging effects during electron beam exposure. A Raith150 Two electron beam lithography (EBL) system was used to expose the nanostructures into the PMMA. Each plasmonic array was patterned within a 40x40 μm^2 area. The main process parameters were 10kV acceleration voltage, 20μm aperture and 110$\mu C/cm^2$ beam dosage. Before development of the PMMA resist, the samples were immersed for 10 s in a gold etchant solution from Sigma-Aldrich, rinsed with deionized water and dried with a nitrogen gun. Development of the resist was achieved by immersing the samples for 60 s in a 1:3 methyl isobutyl ketone (MIBK) and isopropyl alcohol (IPA) solution, followed by a 60 s immersion in IPA and dried using a flow of nitrogen gas. A 5 nm titanium and 30 nm gold layers were deposited using an Edwards Auto 500 electron beam evaporator at a base pressure below 10^{-6} mbar, and using respectively the evaporation rates 0.085 nm/s and 0.22 nm/s. The final process step involved a lift-off of the metallic film around the exposed areas of PMMA. This was achieved by leaving the samples immersed in acetone overnight, followed the application of a 15 s ultrasonic bath, immersion in IPA for another 60 s and dried with a flow of nitrogen gas.

SHG Microscope

SHG microscopy techniques are also the same as seen in Valev, V. K. et al., 2014[26]. Images are collected with a confocal laser scanning microscope, Zeiss LSM 510 META (Jena, Germany). The sample is illuminated by a femtosecond pulsed Ti:Sapphire laser, directed to the sample by a dichroic mirror (HFT KP650) and through a Zeiss 100x Alpha Plan-APOCHROMAT oil objective of numerical aperture 1.46. The fundamental excitation wavelength is 800 nm. After passing through a dichroic mirror (NFT545) and a band-pass filter (BP 390-465), the nonlinear signals (SHG and part of the TPL) are collected by a photomultiplier tube. The image is formed with a scanning speed of 12.8μs for the pixel dwell time; and each frame is scanned 8 times and averaged.

Analysis

The nonlinear microscopy images obtained contain roughly 60 crosses of each type (normal and mirror), with separate images for LCP and RCP illumination. A Python script was used to specify the central regions of 25 crosses, with clearly damaged structured avoided. For each cross, a 5-pixel by 5-pixel square at the defined central region was intensity-averaged. This result was itself then averaged over the 25 selected crosses to obtain a final intensity and statistical uncertainty for a particular orientation of cross (normal or mirror) and input polarization (LCP or RCP). This was done for each of the considered geometries. These intensities and their corresponding uncertainties are used to obtain the results shown in Figure 2b.

1. Collins, J. T. *et al.* Chirality and Chiroptical Effects in Metal Nanostructures: Fundamentals and Current Trends. *Adv. Opt. Mater.* **1700182,** 1700182 (2017).
2. Valev, V. K., Baumberg, J. J., Sibilia, C. & Verbiest, T. Chirality and Chiroptical Effects in Plasmonic Nanostructures: Fundamentals, Recent Progress, and Outlook. *Adv. Mater.* **25,** 2517–2534 (2013).
3. Pendry, J. B. B. A Chiral Route to Negative Refraction. *Science* **306,** 1353–1355 (2004).
4. Khorasaninejad, M. *et al.* Multispectral Chiral Imaging with a Metalens. *Nano Lett.* **16,** 4595–4600 (2016).
5. Farshchi, R., Ramsteiner, M., Herfort, J., Tahraoui, A. & Grahn, H. T. Optical communication of spin information between light emitting diodes. *Appl. Phys. Lett.* **98,** 162508 (2011).
6. Wagenknecht, C. *et al.* Experimental demonstration of a heralded entanglement source. *Nat. Photonics* **4,** 549–552 (2010).
7. Sherson, J. F. *et al.* Quantum teleportation between light and matter. *Nature* **443,** 557–560 (2006).
8. Tang, Y. & Cohen, A. E. Enhanced enantioselectivity in excitation of chiral molecules by superchiral light. *Science* **332,** 333–336 (2011).
9. Hendry, E. *et al.* Ultrasensitive detection and characterization of biomolecules using superchiral fields. *Nat. Nanotechnol.* **5,** 783–787 (2010).
10. Hendry, E., Mikhaylovskiy, R. V., Barron, L. D., Kadodwala, M. & Davis, T. J. Chiral Electromagnetic Fields Generated by Arrays of Nanoslits. *Nano Lett.* **12,** 3640–3644 (2012).
11. Tullius, R. *et al.* 'Superchiral' Spectroscopy: Detection of Protein Higher Order

Hierarchical Structure with Chiral Plasmonic Nanostructures. *J. Am. Chem. Soc.* **137,** 8380–8383 (2015).

12. Zhao, Y. *et al.* Chirality detection of enantiomers using twisted optical metamaterials. *Nat. Commun.* **8,** 14180 (2017).
13. Wu, Z. & Zheng, Y. Moiré Chiral Metamaterials. *Adv. Opt. Mater*. 1700034 (2017). doi:10.1002/adom.201700034
14. Schäferling, M., Dregely, D., Hentschel, M. & Giessen, H. Tailoring enhanced optical chirality: Design principles for chiral plasmonic nanostructures. *Phys. Rev. X* **2,** 31010 (2012).
15. Karimullah, A. S. *et al.* Disposable Plasmonics: Plastic Templated Plasmonic Metamaterials with Tunable Chirality. *Adv. Mater*. **27,** 5610–5616 (2015).
16. Maoz, B. M. *et al.* Amplification of chiroptical activity of chiral biomolecules by surface plasmons. *Nano Lett.* **13,** 1203–1209 (2013).
17. Wang, R.-Y. R. Y. *et al.* Experimental Observation of Giant Chiroptical Amplification of Small Chiral Molecules by Gold Nanosphere Clusters. *J. Phys. Chem. C* **118,** 9690–9695 (2014).
18. Ma, W. *et al.* Attomolar DNA detection with chiral nanorod assemblies. *Nat. Commun.* **4,** 2689 (2013).
19. Zhang, H. & Govorov, A. O. Giant circular dichroism of a molecule in a region of strong plasmon resonances between two neighboring gold nanocrystals. *Phys. Rev. B* **87,** 75410 (2013).
20. Zu, S., Bao, Y. & Fang, Z. Planar Plasmonic Chiral Nanostructures. *Nanoscale* **8,** 3900–3905 (2016).

21. Valev, V. K. Characterization of nanostructured plasmonic surfaces with second harmonic generation. *Langmuir* **28,** 15454–15471 (2012).

22. Wang, T., Halaney, D., Ho, D., Feldman, M. D. & Milner, T. E. Two-photon luminescence properties of gold nanorods. *Biomed. Opt. Express* **4,** 584 (2013).

23. Chen, C. K., Heinz, T. F., Ricard, D. & Shen, Y. R. Surface-enhanced second-harmonic generation and Raman scattering. *Phys. Rev. B* **27,** 1965–1979 (1983).

24. Valev, V. K. *et al.* Hotspot Decorations Map Plasmonic Patterns with the Resolution of Scanning Probe Techniques. *Phys. Rev. Lett.* **106,** 226803 (2011).

25. Valev, V. K. *et al.* Plasmonic Ratchet Wheels: Switching Circular Dichroism by Arranging Chiral Nanostructures. *Nano Lett.* **9,** 3945–3948 (2009).

26. Valev, V. K. *et al.* Nonlinear Superchiral Meta-Surfaces: Tuning Chirality and Disentangling Non-Reciprocity at the Nanoscale. *Adv. Mater.* **26,** 4074–4081 (2014).

27. Petralli-Mallow, T., Wong, T. M., Byers, J. D., Yee, H. I. & Hicks, J. M. Circular dichroism spectroscopy at interfaces: a surface second harmonic generation study. *J. Phys. Chem.* **97,** 1383–1388 (1993).

28. Byers, J. D., Yee, H. I. & Hicks, J. M. A second harmonic generation analog of optical rotatory dispersion for the study of chiral monolayers. *J. Chem. Phys.* **101,** 6233 (1994).

29. Vandenbosch, G. A. E. & Van de Capelle, A. R. Mixed-potential integral expression formulation of the electric field in a stratified dielectric medium-application to the case of a probe current source. *IEEE Trans. Antennas Propag.* **40,** 806–817 (1992).

30. Demuynck, F. J., Vandenbosch, G. A. E. & Van De Capelle, A. R. The expansion wave concept-Part I: Efficient calculation of spatial green's functions in a stratified dielectric medium. *IEEE Trans. Antennas Propag.* **46,** 397–406 (1998).

31. Vrancken, M. & Vandenbosch, G. A. E. Hybrid dyadic-mixed-potential and combined spectral-space domain integral-equation analysis of quasi-3-D structures in stratified media. *IEEE Trans. Microw. Theory Tech.* **51,** 216–225 (2003).

32. Schols, Y. & Vandenbosch, G. A. E. Separation of Horizontal and Vertical Dependencies in a Surface/Volume Integral Equation Approach to Model Quasi 3-D Structures in Multilayered Media. *IEEE Trans. Antennas Propag.* **55,** 1086–1094 (2007).

33. Vandenbosch, G. A. E., Volski, V., de Arquer, F. P. G., Verellen, N. & Moshchalkov, V. On the use of the Method of Moments in plasmonic applications. in *2010 URSI International Symposium on Electromagnetic Theory* **46,** 257–260 (IEEE, 2010).

34. Zheng, X. *et al.* Volumetric method of moments and conceptual multilevel building blocks for nanotopologies. *IEEE Photonics J.* **4,** 267–282 (2012).

35. Zheng, X. *et al.* Interacting plasmonic nanostructures beyond the quasi-static limit: a 'circuit' model. *Opt. Express* **21,** 31105 (2013).

36. Zheng, X. *et al.* On the Use of Group Theory in Understanding the Optical Response of a Nanoantenna. *IEEE Trans. Antennas Propag.* **63,** 1589–1602 (2015).

37. Li, W. *et al.* Circularly polarized light detection with hot electrons in chiral plasmonic metamaterials. *Nat. Commun.* **6,** 8379 (2015).

38. Lee, S. *et al.* Circular dichroism in planar extrinsic chirality metamaterial at oblique incident beam. *Opt. Commun.* **309,** 201–204 (2013).

39. Decker, M., Klein, M. W., Wegener, M. & Linden, S. Circular dichroism of planar chiral magnetic metamaterials. *Opt. Lett.* **32,** 856–858 (2007).

40. Droulias, S. & Yannopapas, V. Broad-Band Giant Circular Dichroism in Metamaterials of Twisted Chains of Metallic Nanoparticles. *J. Phys. Chem. C* **117,** 1130–1135 (2013).

41. Plum, E., Fedotov, V. a & Zheludev, N. I. Extrinsic electromagnetic chirality in metamaterials. *J. Opt. A Pure Appl. Opt.* **11,** 74009 (2009).

42. Kuhn, W. The physical significance of optical rotatory power. *Trans. Faraday Soc.* **26,** 293 (1930).

43. Guerrero-Martínez, A. *et al.* Intense Optical Activity from Three-Dimensional Chiral Ordering of Plasmonic Nanoantennas. *Angew. Chemie Int. Ed.* **50,** 5499–5503 (2011).

44. Fan, Z. & Govorov, A. O. Plasmonic Circular Dichroism of Chiral Metal Nanoparticle Assemblies. *Nano Lett.* **10,** 2580–2587 (2010).

45. Auguié, B., Alonso-Gómez, J. L., Guerrero-Martínez, A. & Liz-Marzán, L. M. Fingers Crossed: Optical Activity of a Chiral Dimer of Plasmonic Nanorods. *J. Phys. Chem. Lett.* **2,** 846–851 (2011).

46. Hentschel, M., Ferry, V. E. & Alivisatos, A. P. Optical Rotation Reversal in the Optical Response of Chiral Plasmonic Nanosystems: The Role of Plasmon Hybridization. *ACS Photonics* **2,** 1253–1259 (2015).

47. Pendry, J. B. Negative Refraction Makes a Perfect Lens. *Phys. Rev. Lett.* **85,** 3966–3969 (2000).

48. Fang, N. Sub-Diffraction-Limited Optical Imaging with a Silver Superlens. *Science* **308,** 534–537 (2005).

49. Ono, A., Kato, J. & Kawata, S. Subwavelength Optical Imaging through a Metallic Nanorod Array. *Phys. Rev. Lett.* **95,** 267407 (2005).

50. Synge, E. H. XXXVIII. A suggested method for extending microscopic resolution into the ultra-microscopic region. *London, Edinburgh, Dublin Philos. Mag. J. Sci.* **6,** 356–362 (1928).

51. Narushima, T. & Okamoto, H. Circular dichroism nano-imaging of two-dimensional chiral metal nanostructures. *Phys. Chem. Chem. Phys.* **15,** 13805 (2013).

52. Narushima, T. & Okamoto, H. Strong Nanoscale Optical Activity Localized in Two-Dimensional Chiral Metal Nanostructures. *J. Phys. Chem. C* **117,** 23964–23969 (2013).

53. Narushima, T., Hashiyada, S. & Okamoto, H. Nanoscopic Study on Developing Optical Activity with Increasing Chirality for Two-Dimensional Metal Nanostructures. *ACS Photonics* **1,** 732–738 (2014).

54. Okamoto, H., Narushima, T., Nishiyama, Y. & Imura, K. Local optical responses of plasmon resonances visualised by near-field optical imaging. *Phys. Chem. Chem. Phys.* **17,** 6192–6206 (2015).

55. Narushima, T., Hashiyada, S. & Okamoto, H. Optical Activity Governed by Local Chiral Structures in Two-Dimensional Curved Metallic Nanostructures. *Chirality* **28,** 540–544 (2016).

56. Hashiyada, S., Narushima, T. & Okamoto, H. Local Optical Activity in Achiral Two-Dimensional Gold Nanostructures. *J. Phys. Chem. C* **118,** 22229–22233 (2014).

57. Denkova, D. *et al.* Mapping Magnetic Near-Field Distributions of Plasmonic Nanoantennas. *ACS Nano* **7,** 3168–3176 (2013).

58. Aksyutov, L. N. Temperature dependence of the optical constants of tungsten and gold. *J. Appl. Spectrosc.* **26,** 656–660 (1977).

Funding Sources

VKV acknowledges support from the Royal Society through the University Research Fellowships. The authors would like to acknowledge the C2 project (C24/15/015) and the PDMK/14/126 project of KU Leuven, the FWO long term stay abroad project grant V405115N, and the Methusalem project funded by the Flemish government. We are grateful to Mr Tao Hongjian, Counsellor in the Education Section of the Embassy of the People's Republic of China in the Kingdom of Belgium, for facilitating the collaboration between the UK, Chinese and Belgian teams.

Corresponding Author

* xuezhi.zheng@esat.kuleuven.be, v.k.valev@bath.ac.uk

Author contributions

Experiments were planned by VKV. Samples were prepared by NB and PAW. Experiments were executed by VKV, ES and MA. The data were analyzed by JTC and VKV. The theoretical part, as well as near-field and scattering simulations were performed by XZ and GAEV. Numerical simulations of the far-field, linear CD were performed by SZ and ZF. JTC produced the first draft and all authors contributed to the manuscript.

Figures

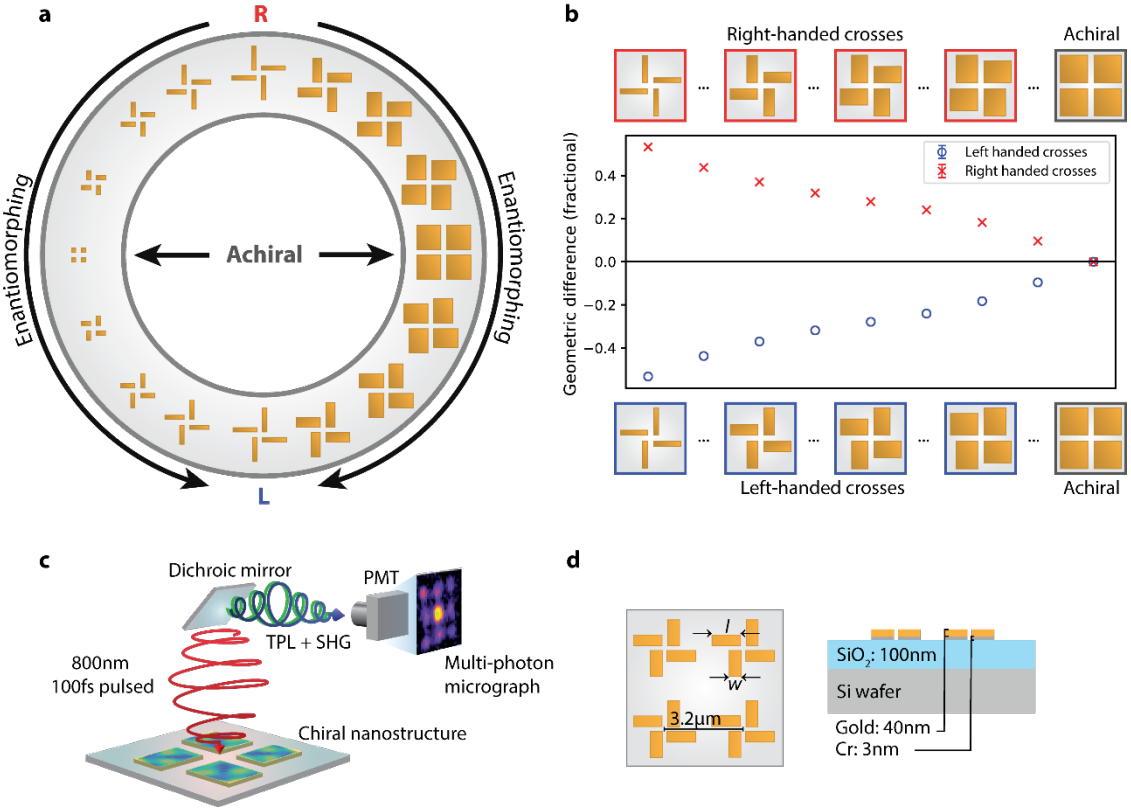

Figure 1. a. Representation of two possible pathways to enantiomorph a right-handed structure (R) into a left-handed structure (L), through an achiral geometry. Here we examine the pathway on the right side of the circle. **b**. As the left handed chiral crosses change into achiral square structures and into right handed chiral crosses, the chiral geometric difference diminishes until it reaches 0 in the achiral case and then reverse its value. **c**. Schematic diagram of the multiphoton microscopy experiments. **d**. Geometry and depth profile of the chiral crosses samples.

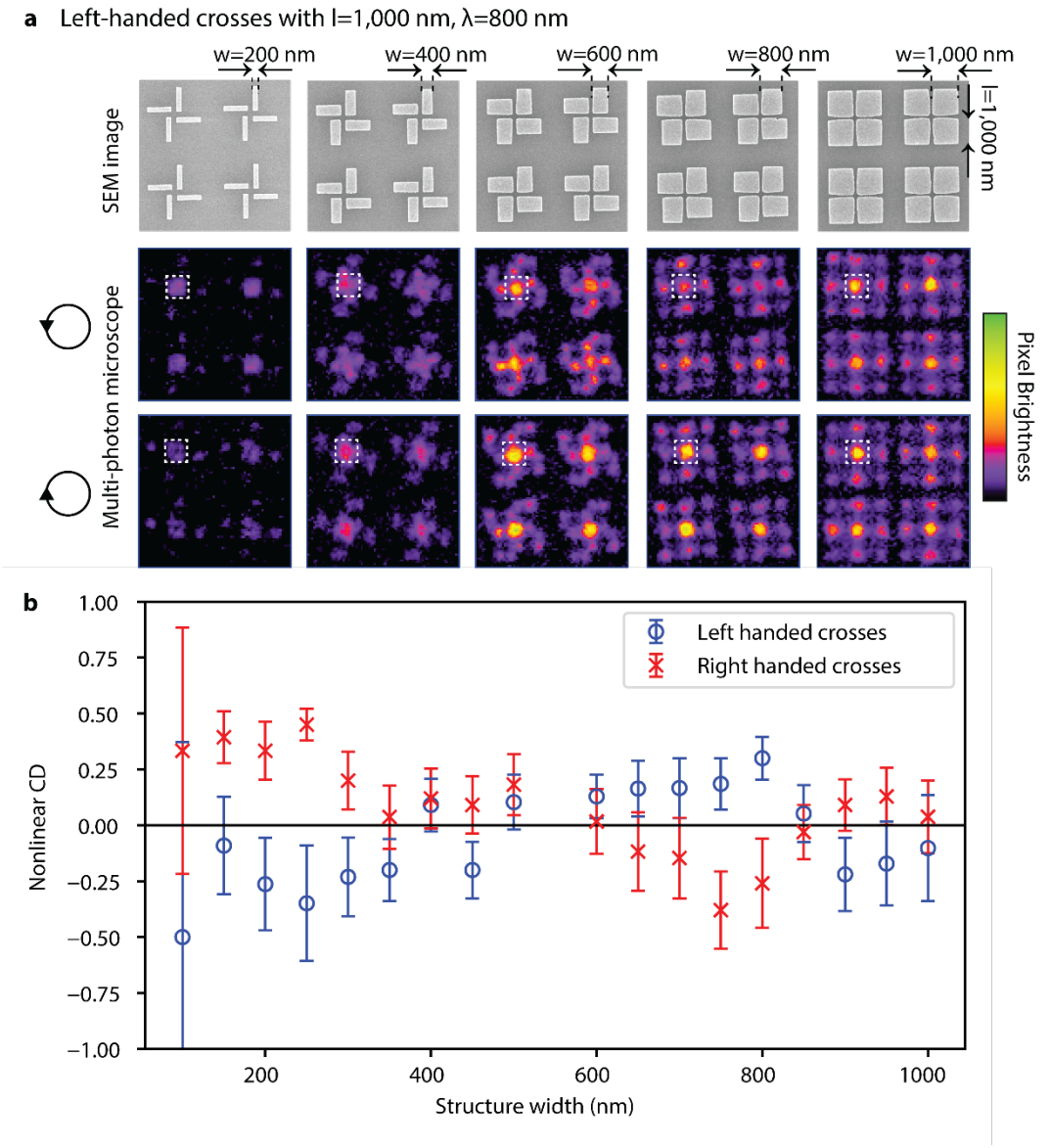

Figure 2. Varying arm width of the nanostructure features at fixed *l*=1000nm. SEM images of 4 structure cells for each geometry (**a**, top), and SHG microscopy images (**a**, lower) under illumination from left and right circularly polarized light, at 800nm wavelength. Scale (right) corresponds to image pixel brightness. **b.** Measured total nonlinear CD under 800nm wavelength light is then calculated for each geometry. Our experiments reveal a counter-intuitive behavior for the second-harmonic generation circular dichroism (SHG-CD) – both the 0 value and the reversal occur before reaching the achiral geometry.

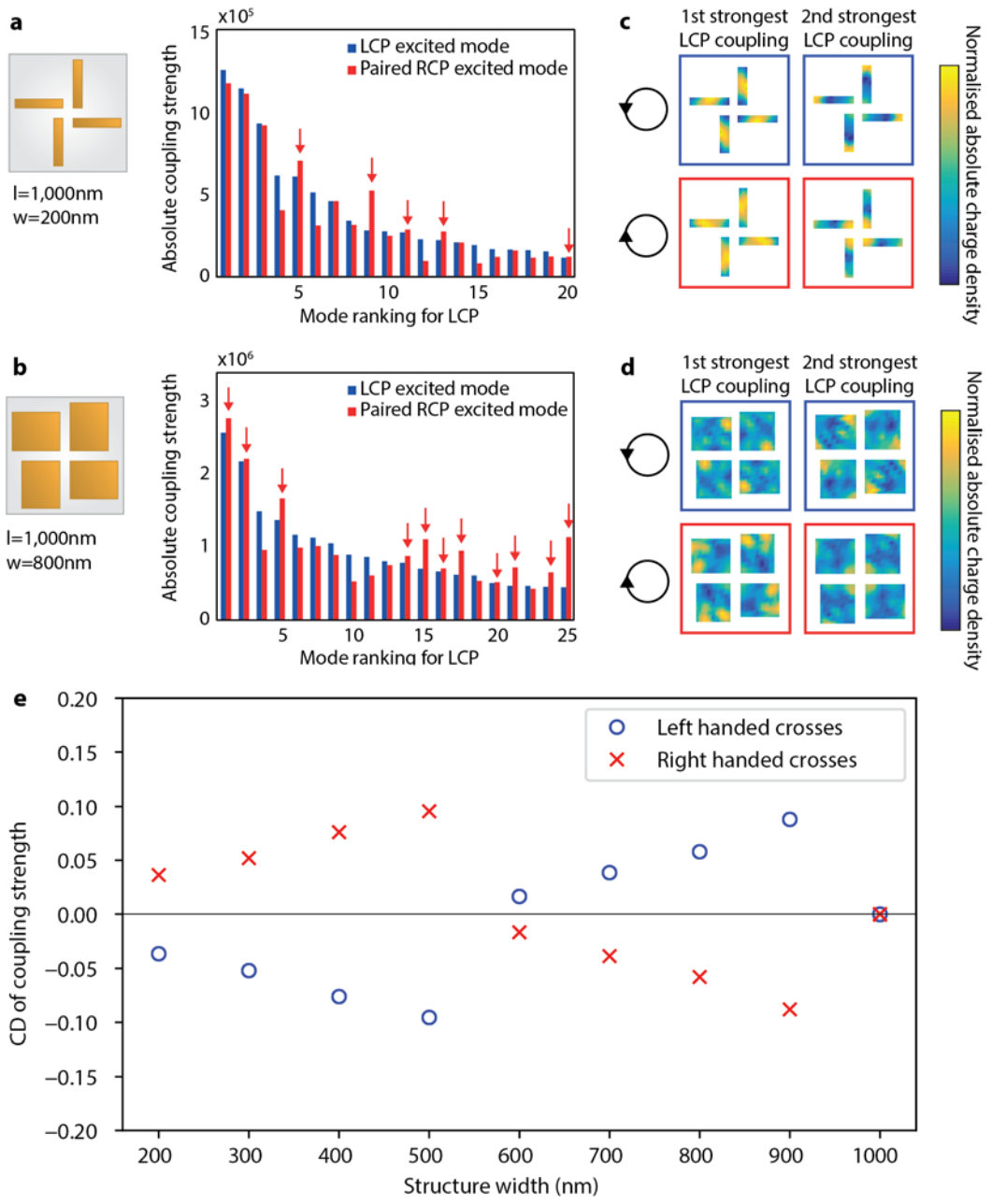

Figure 3. Simulation results showing modal composition of chiroptical response. Modal analysis of structures with arm length 1000nm, width 200nm (**a**) and 800nm (**b**). The most LCP-dominant modes for each structure are plotted showing both LCP coupling strength (blue) and the correlated-mode RCP coupling strength (red). Modes coupling stronger to RCP than LCP are marked with

arrows. Examples of individual modes (normalized absolute charge density) are shown for width 200nm (**c**) and 800nm (**d**)**.** The total coupling strength CD as defined in equation (6) is plotted for varying arm width, at fixed *l*=1000nm under 800nm wavelength light (**e**).

Supplementary Figures

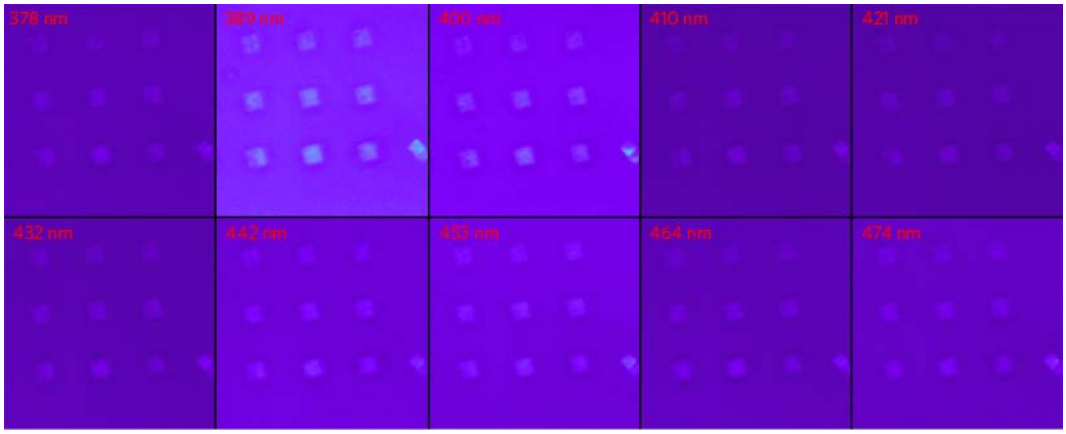

Figure 1. **SHG and TPL emission from cross structures.** Multiphoton microscopy images for *l*=1000 nm, *w*=800 nm cross structures. Centre-to-centre spacing between structures is 2.4 μm. The colour scale (rainbow, from violet to red) is proportional to the intensity of multiphoton emission. Clear SHG enhancement can be seen in 389 nm and 400 nm regions, with TPL showing an identical spatial response at other wavelengths.

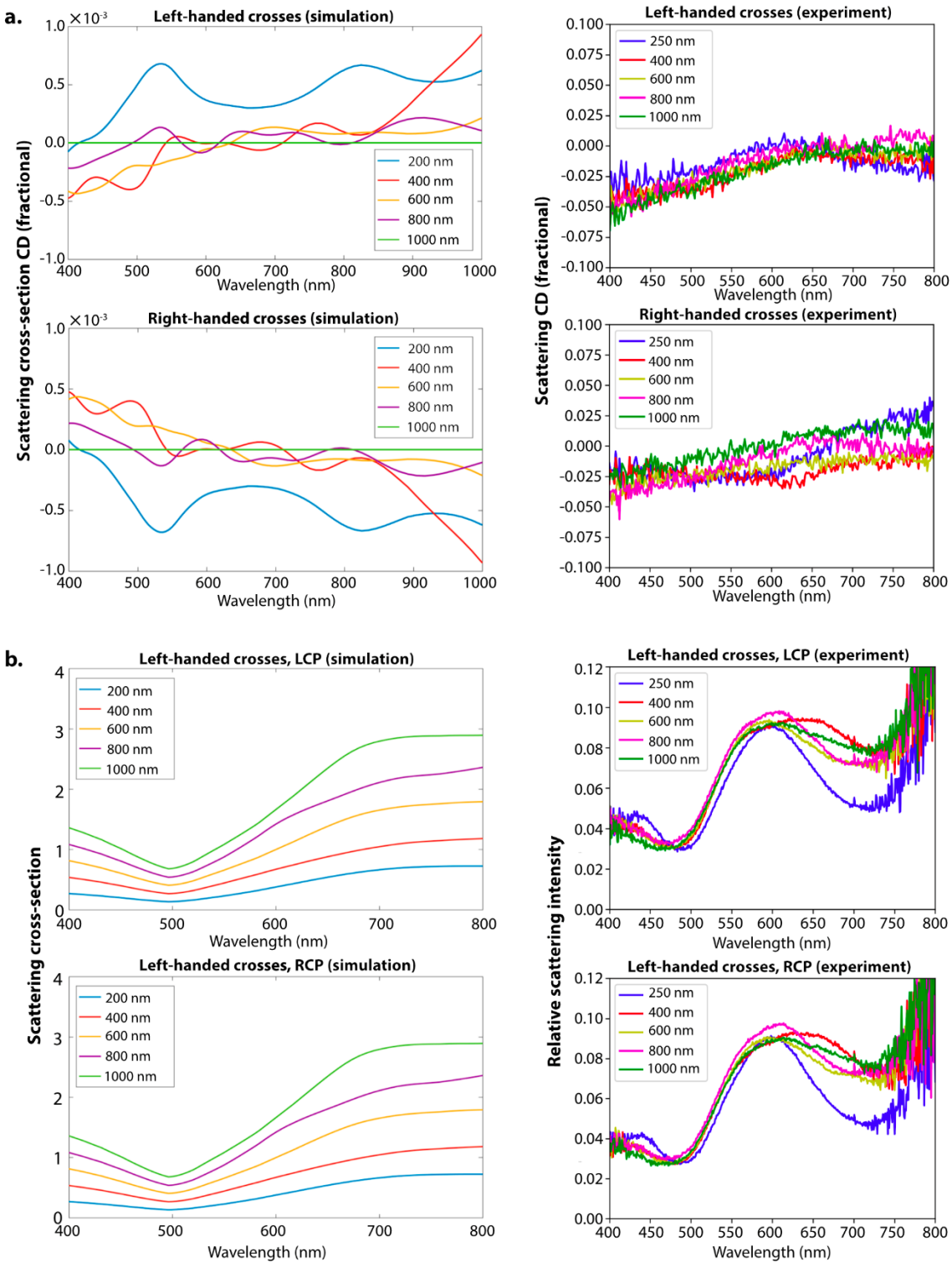

Figure 2. CD in linear scattering cross section for *l*=1000 nm structures. a. (Left) Numerically-obtained linear scattering CD for left-handed (top) and right-handed (bottom) chiral cross structures, with varying nanostripe width (legend). **(Right)** Experimentally obtained linear scattering CD for the same structures. **b. (Left)** Numerically-obtained linear scattering cross sections for left-handed chiral cross structures under LCP (top) and RCP (bottom) illumination, with varying arm width (legend). **(Right)** Experimentally obtained linear scattering spectra for the same structures.

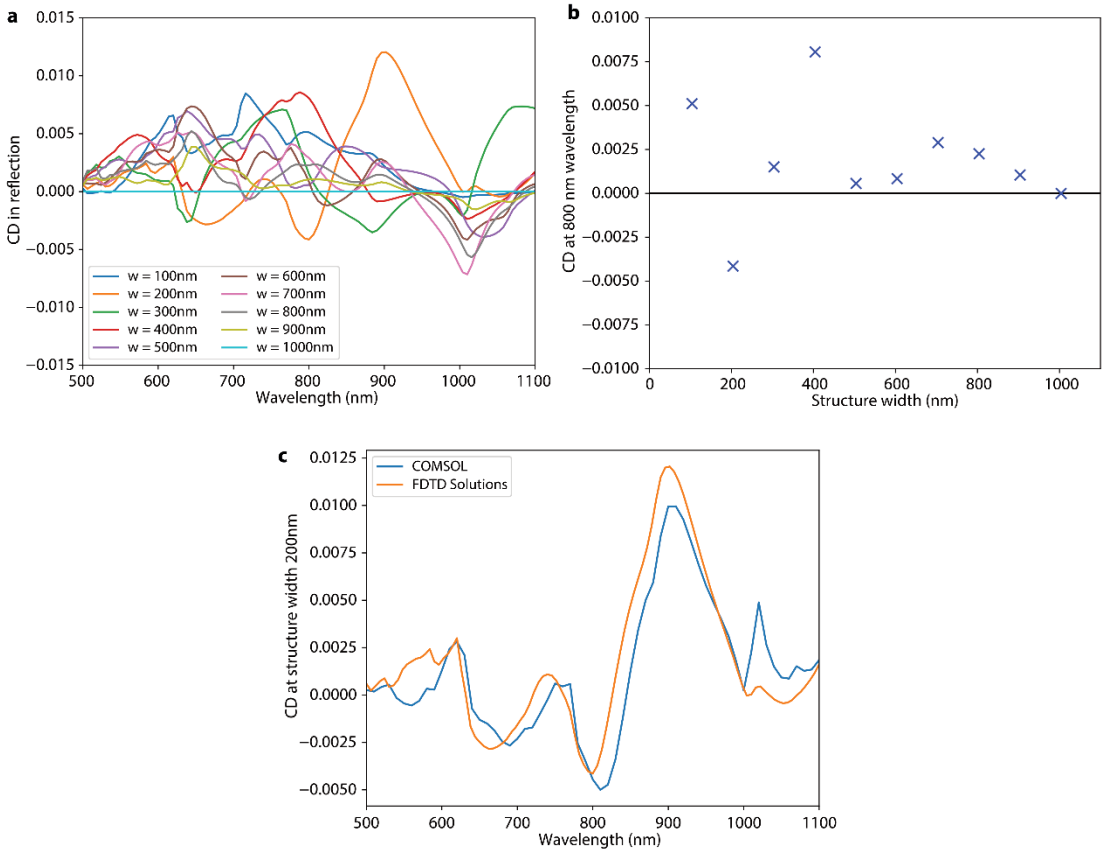

Figure 3. CD in reflection for l=1000nm structures. a. Numerically-obtained reflection CD spectra for left-handed chiral cross structures, with varying arm width (legend). No systematic shift of the spectral response is observed when changing the nanostructure dimensions. **b.** Linear CD with varying arm width at 800nm incident light, obtained from spectra shown in a. The lineshape of the CD response is drastically different to that obtained from nonlinear CD measurements. **c.** Comparison of two numerical methods used to obtain CD spectra for w=200 nm structure; FDTD Solutions, and COMSOL Multiphysics. Overall shape of CD response is in good agreement between the two methods.

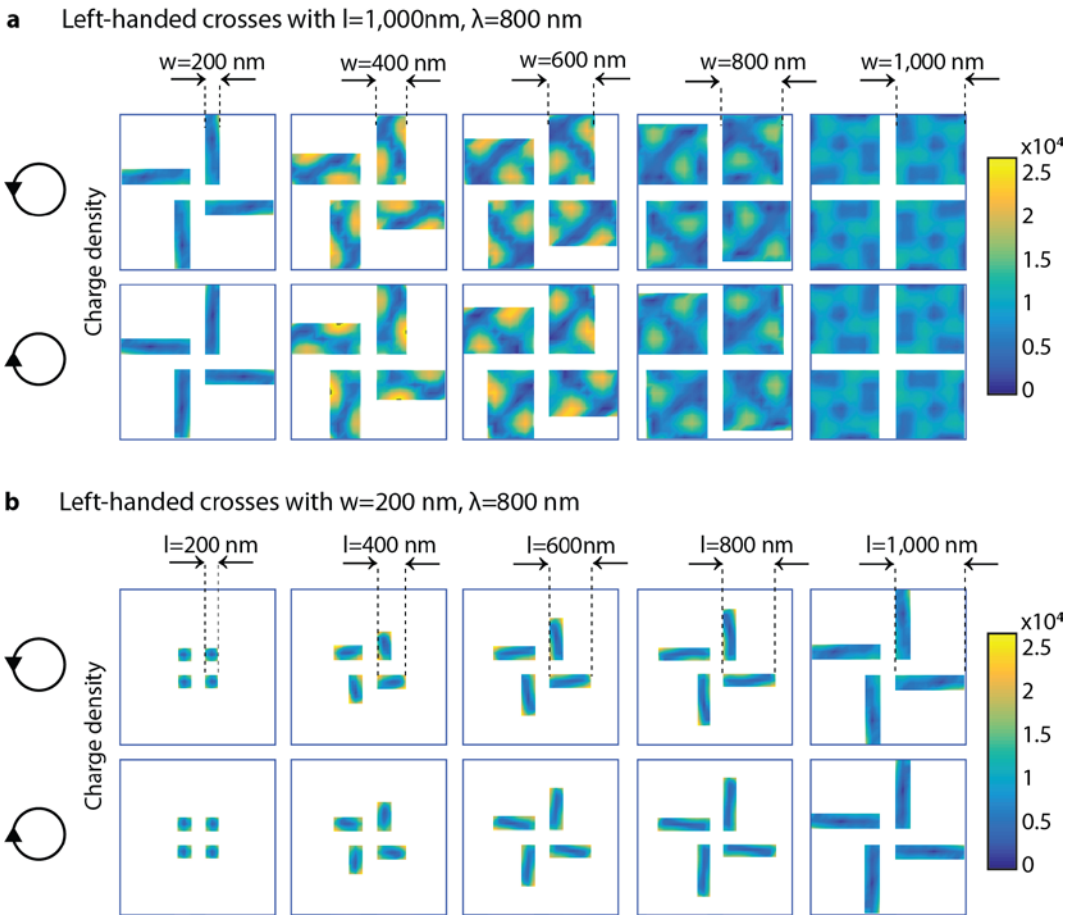

Figure 4. Full charge density solutions. Calculated for both LCP and RCP 800nm incident light, for varying arm width of the nanostructure features at fixed l=1000 nm (**a**) and varying arm length of the nanostructure features at fixed d=200 nm (**b**). Full solution is calculated by linearly superposing the contributions from all the eigenmodes $\boldsymbol{J_n}$.

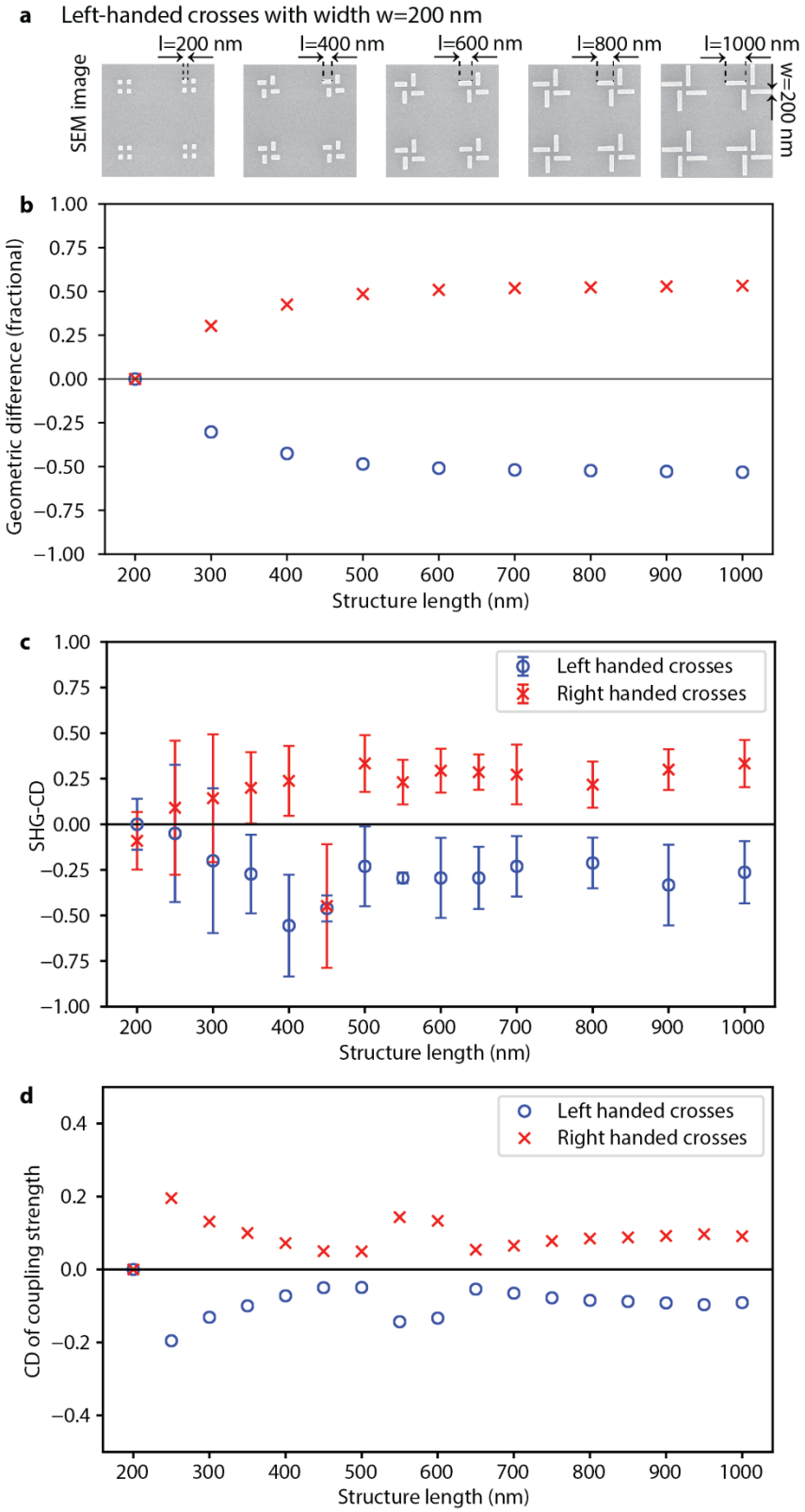

Figure 5. Additional experimental and simulated CD results. Varying arm length of the nanostructure features at fixed *w*=200 nm. **a.** SEM images of 4 structure cells for each geometry. **b.** Chiral geometric difference for structures of fixed arm width *w*=200 nm. Measured total multi-photon CD (**c**), and total coupling strength CD (**d**), under 800 nm wavelength light is then calculated for each geometry. Unlike the case of fixed length and varying width, no bisignate CD is observed here.

Supplementary Discussion

Supplementary Discussion 1: Formulating the interaction of light with a nanoscatterer in the framework of a Volume Integral Equation (VIE)

In the following, we discuss a Volume Integral Equation (VIE) formalism for light – nanostructure interactions. This material can also be found in our previous work [1]. It is reviewed here only for the sake of completeness. The physical process governing the interaction between light and a general scatterer can be described by the following two equations in the frequency domain,

$$\mathbf{E}_{\mathbf{tot}}\left(\mathbf{r}\right)=\mathbf{E}_{\mathbf{inc}}\left(\mathbf{r}\right)+\mathbf{E}_{\mathbf{scat}}\left(\mathbf{r}\right),\ \mathbf{E}_{\mathbf{scat}}\left(\mathbf{r}\right)=i\omega\mu_0\mu_1\int_V\vec{G}\left(\mathbf{r},\mathbf{r}'\right)\cdot\mathbf{J}\left(\mathbf{r}'\right)dv'. \tag{1}$$

In equation (1), the first equation simply states that everywhere in space the total electric field is the sum of the *impressed* incident field and the scattered field. This scattered field is generated by the induced currents flowing in the source volume, which gives the gist of the second equation in equation (1). Here, μ_0 and μ_1 are the vacuum permeability and the relative permeability of the material filling the space where the scatterer is situated. $\bar{G}(\mathbf{r},\mathbf{r}')$ is the electric dyadic Green's function. Please note that in this article a $e^{-i\omega t}$ time convention is employed and the angular frequency ω has been systematically suppressed. Especially at the spatial position of the scatterer, the total field is linked with the induced current via,

$$\mathbf{E}_{\mathbf{tot}}\left(\mathbf{r}\right)=\frac{\mathbf{J}\left(\mathbf{r}\right)}{-i\omega\varepsilon_0\left(\varepsilon_r\left(\omega\right)-1\right)},\ \mathbf{r}\in V. \tag{2}$$

V in equation (1) and equation (2) denotes the source volume. In equation (2), ε_0 and $\varepsilon_r(\omega)$ represent the vacuum permittivity and the relative permittivity of the material that constitutes the scatterer. Combining the above equations, we have

$$\frac{\mathbf{J}\left(\mathbf{r}\right)}{-i\omega\varepsilon_0\left(\varepsilon_r\left(\omega\right)-1\right)}-i\omega\mu_0\mu_1\int_V\vec{G}\left(\mathbf{r},\mathbf{r}'\right)\cdot\mathbf{J}\left(\mathbf{r}'\right)dv'=\mathbf{E}_{\mathbf{inc}}\left(\mathbf{r}\right),\ \mathbf{r}\in V. \tag{3}$$

In equation (3), since the incident electric field and the electric dyadic Green's function are assumed to be known in the first place, the induced current is the main target to solve and can be numerically evaluated by, e.g. a Method of Moments (MoM) algorithm. Writing compactly, we have the following operator formalism as in the main text,

$$Z\left(\mathbf{r},\mathbf{r}';\omega\right)\cdot\mathbf{J}\left(\mathbf{r}',\omega\right)=\mathbf{E}_{\mathbf{inc}}\left(\mathbf{r},\omega\right). \tag{4}$$

In equation (4), the impedance operator $\mathbf{Z}(\boldsymbol{r},\boldsymbol{r}';\omega)$ is

$$Z\left(\mathbf{r},\mathbf{r}';\omega\right)=\frac{1}{-i\omega\varepsilon_0\left(\varepsilon_r\left(\omega\right)-1\right)}\delta\left(\mathbf{r}-\mathbf{r}'\right)-i\omega\mu_0\mu_1\int_V\vec{G}\left(\mathbf{r},\mathbf{r}'\right)\cdot\ dv'. \tag{5}$$

A Dirac delta is added in equation (5) to emphasize the local approximation.

Supplementary Discussion 2: Modes and Symmetry in 4I Structures

In the following numerical analysis, the in-principle infinite dimensional impedance operator **Z** is approximated by a finite dimensional one, that is, a matrix. Since our discussions are actually conducted with respect to this matrix, here after we will use the terms operator and matrix interchangeably.

Symmetry and a Group Representation Theoretical Approach

Aside from all the differences in dimensions, the structures' symmetry is unchanged. That is, all the structures carry a C_4 symmetry group (see the symmetry operations in **Supplementary Figure 6a**). There are four symmetry operations in this group: the identity operation E where no transformation is conducted, a rotation of $\frac{\pi}{2}$, a rotation of π and a rotation of $\frac{3\pi}{2}$. All of these rotations are about the z axis and are named as C_4^1, C_4^2, and C_4^3.

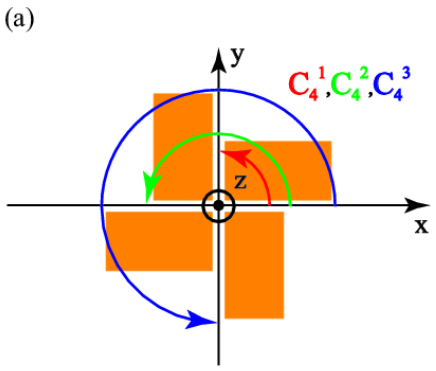

(b)

	Γ_1	Γ_2	Γ_3	Γ_4
E	+1	+1	+1	+1
C_4^1	+1	-1	+1	-1
C_4^2	+1	+i	-1	-i
C_4^3	+1	-i	-1	+i

Supplementary Figure 6 Illustration of the symmetry operations and the irreducible representation for the C_4 group. **a,** demonstrates the symmetry operations for a 4I chiral structure. These symmetry operations form a group and the irreducible representations of the group are shown in **b**.

Since symmetry operations are always applied based on coordinates, we should be able to find a corresponding set of matrices to "represent" these operations. Here, we especially focus on the matrices with the lowest dimensionalities, that is, the irreducible representations. Since the group under discussion is an Abelian group, we have four irreducible representations and they are shown in **Supplementary Figure 6b**. Moreover, in contrast to these transformations operating on coordinates, we follow Wigner's conventions [2–4] and define transformation operators which operate on functions,

$$P_R f(\mathbf{r}) = f\left(R^{-1}\mathbf{r}\right),\ P_R \mathbf{f}(\mathbf{r}) = R \cdot \mathbf{f}\left(R^{-1}\mathbf{r}\right). \tag{6}$$

In equation (6), this definition is illustrated for both scalar functions (such as charge, etc.) and vector functions (such as currents, electromagnetic fields, etc.). These transformation operators are commutative with the impedance operator $\mathbf{Z}(\boldsymbol{r}, \boldsymbol{r}'; \omega)$ (see proof in Supplementary

Discussion 3) used in the electric field volume integral equation,

$$Z\left(\mathbf{r},\mathbf{r}';\omega\right)\cdot\mathbf{J}\left(\mathbf{r}',\omega\right)=\mathbf{E}_{\mathbf{inc}}\left(\mathbf{r},\omega\right). \tag{7}$$

Combining the group's irreducible representations and its transformation operators, we can further construct a set of projection operators [2–4] for the group under discussion,

$$\mathcal{P}_j=\frac{l_j}{h}\sum_R\Gamma_j\left(R\right)^*P_R. \tag{8}$$

In equation (8), a projection operator is characterized by the subscript j which marks an irreducible representation. Here, j may run from one to four. l_j is the dimensionality for an irreducible representation and since every irreducible representation has a dimensionality of one, l_j is equal to one. Then, the summation is carried out with respect to all the symmetry operations.

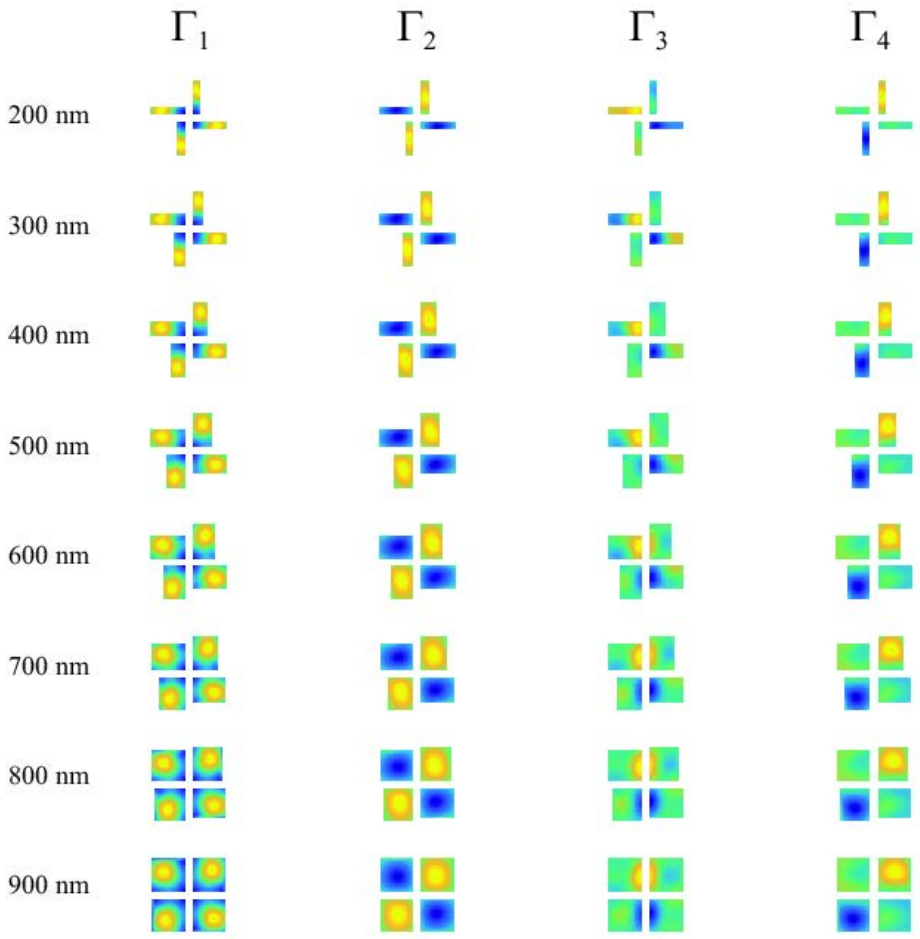

Supplementary Figure 7 Illustration of exemplary eigenmodes for the 4I structures. In the columns, we find eigenmodes that belong to the same irreducible representation. In all the plots, the top surface charge is shown and coded by the blue color and the yellow color to represent the negative and positive charge accumulations.

A Mix of Modes and Symmetry: A Group Theoretical Approach

Now, we are ready to combine the above discussions on the eigenvalue problem with group

representation theory. On the one hand, all the eigenmodes can be categorized according to the irreducible representations (and hence the projection operators). Notice that in equation (8) the j^{th} projection operator is defined for the j^{th} irreducible representation [3,4], see an illustration of eigenmode categorization in **Supplementary Figure 7**. It is also known that the functions (for example, in the current case, the eigenmodes) that belong to different irreducible representations are orthogonal to each other in an inner product sense [2–4]. The above is equivalent to saying that, according to irreducible representations, an eigenspace (in which one finds all the eigenmodes) can be split into several invariant subspaces (in which one finds all the eigenmodes belonging to an irreducible representation).

On the other hand, we apply the projection operators to both sides of equation (7),

$$\mathcal{P}_j Z J = \mathcal{P}_j E \Leftrightarrow Z \mathcal{P}_j J = \mathcal{P}_j E \Leftrightarrow Z J_j = E_j. \tag{9}$$

In equation (9), the second step is established because the projection operator is a weighted sum of the transformation operators (see equation (8)) and the transformation operators (as defined in equation (6)) are commutative with the impedance operator. J_j and E_j are projected full solution currents and excitations due to the j^{th} irreducible representation. equation (9) actually states that only the current and excitation that belong to the same irreducible representation are coupled with each other. Take the "left" structure excited by a left polarized light as an example. In **Supplementary Figure 8**, we demonstrate the absolute value of the top surface charge distribution (see **Supplementary Figure 8a**) and the 2-norm of the projected excitation (see **Supplementary Figure 8b**). There, it can be readily seen that since the excitation solely contains a component that belongs to the 3rd irreducible representation, only the current associated with the same irreducible representation is excited.

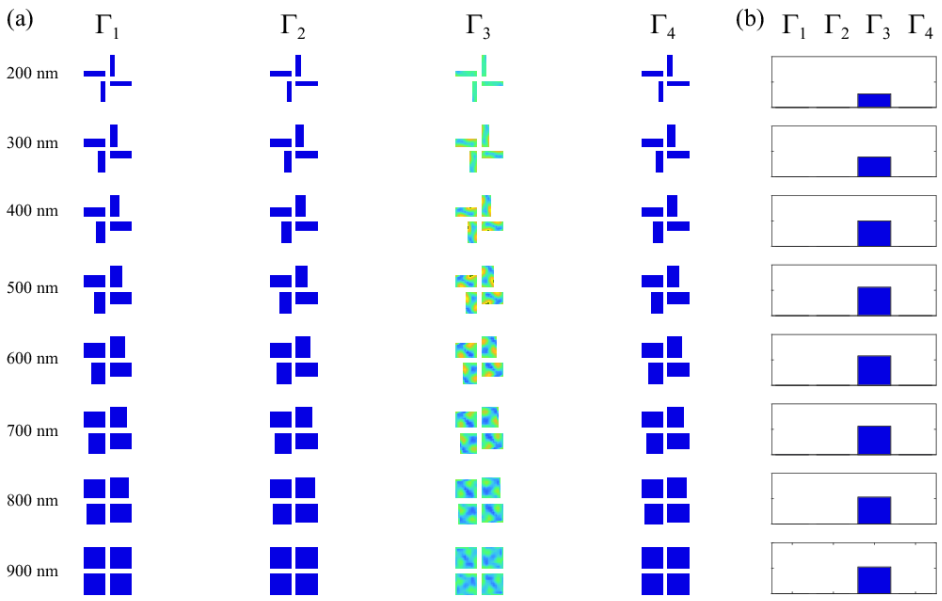

Supplementary Figure 8 Illustration of projected full solutions (**a**) and the norm of the projected excitations (**b**) for the "left" structure. In (**a**), the color is coded from blue to yellow to represent the absolute value of the top surface charge distribution. In all the subplots of (**a**), the same color scale is employed.

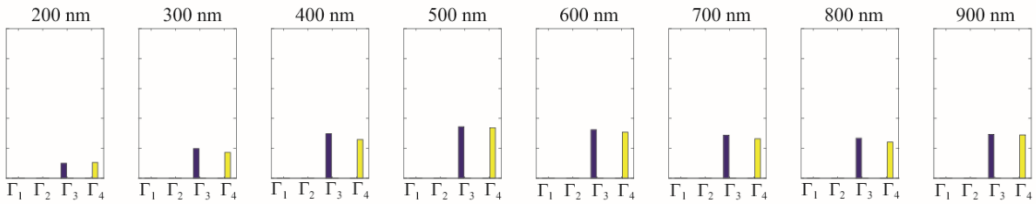

Supplementary Figure 9 Illustration of coupling coefficients of the left circularly polarized light (LCP, the blue bar) and the right circularly polarized light (RCP, the yellow bar) for the "left" structure.

Again, since the projected currents or the projected excitations belong to different irreducible representations, they are orthogonal to each other. As a result, the projected currents can only be reconstructed by the eigenmodes associated with the same irreducible representation. Hence, we can rewrite

$$\mathbf{J}(\mathbf{r}',\omega) = \sum c_n(\omega)\mathbf{J}_\mathbf{n}(\mathbf{r}',\omega) \tag{10}$$

as

$$\mathbf{J}_j(\mathbf{r}',\omega) = \sum c_{j,n}(\omega)\mathbf{J}_{j,\mathbf{n}}(\mathbf{r}',\omega). \tag{11}$$

In equation (11), j represents a certain irreducible representation. In **Supplementary Figure 9**, for an irreducible representation, a sum is taken for the absolute value of all the coupling coefficients of the eigenmodes that are associated with this irreducible representation. It can be immediately seen from this figure that when a left circularly polarized light is used to irradiate the "left" structures, only the eigenmodes (the sum of whose coupling coefficients is marked by the blue strip) that belong to the 3rd irreducible representation are excited. However, when a right circularly polarized light is employed, only the eigenmodes (the sum of whose coupling coefficients is marked by the yellow strip) that are associated with the 4th irreducible representation are stimulated.

Supplementary Discussion 3: On the commutative relation between an impedance operator and transformation operators

In this section, we prove the fact the impedance operator $\mathbf{Z}(\mathbf{r}, \mathbf{r}'; \omega)$ defined by,

$$Z\left(\mathbf{r},\mathbf{r}';\omega\right)\cdot\mathbf{J}\left(\mathbf{r}',\omega\right)=\mathbf{E}_{\mathbf{inc}}\left(\mathbf{r},\omega\right) \tag{12}$$

is indeed commutative with a transformation operator,

$$Z\left(\mathbf{r},\mathbf{r}';\omega\right)\cdot P_R\mathbf{J}\left(r'\right)=P_R Z\left(\mathbf{r},\mathbf{r}';\omega\right)\cdot\mathbf{J}\left(r'\right). \tag{13}$$

As we consider a specific frequency, in the following we will systematically suppress the frequency variable appearing in equation (5). We assume that the targeted structure holds some symmetry operation *R*. In accordance with this symmetry operation we can define a transformation operator which works on functions, for example, the current in equation (4),

$$P_R\mathbf{J}\left(\mathbf{r}'\right)=R\cdot\mathbf{J}\left(R^{-1}\mathbf{r}'\right). \tag{14}$$

In this work the structure is put on top of a glass substrate occupying the lower half space. Consequently, the symmetry operation and its corresponding transformation operator are actually confined to the *x*-*y* plane. For example, the symmetry operation can be represented by a matrix,

$$R=\begin{pmatrix} R_{xx} & R_{xy} & 0 \\ R_{yx} & R_{yy} & 0 \\ 0 & 0 & 1 \end{pmatrix}. \tag{15}$$

Especially, here we focus on two types of elementary transformations in the *x*-*y* plane: rotations about the origin by an angle θ and reflections about a line which makes an angle θ with the *x* axis,

$$R_{rot}=\begin{pmatrix} \cos\theta & -\sin\theta & 0 \\ \sin\theta & \cos\theta & 0 \\ 0 & 0 & 1 \end{pmatrix},\ R_{refl}=\begin{pmatrix} \cos 2\theta & \sin 2\theta & 0 \\ \sin 2\theta & -\cos 2\theta & 0 \\ 0 & 0 & 1 \end{pmatrix}. \tag{16}$$

In equation (16), the matrices are orthogonal matrices with a determinant either +1 or -1. Other more complex transformations, for example, inversions, can be constructed by combining the above two elementary operations.

Moreover, due to the presence of the lower half space, we can split the dyadic Green's function in equation (5) into two parts, that is, a direct wave part and a reflected wave part,

$$\overline{G}\left(\mathbf{r},\mathbf{r}'\right)=\overline{G}_0\left(\mathbf{r},\mathbf{r}'\right)+\overline{G}_r\left(\mathbf{r},\mathbf{r}'\right). \tag{17}$$

For the direct field part, a closed form expression in the spatial domain is

$$\overline{G}_0(\mathbf{r},\mathbf{r}') = \left[I + \frac{\nabla\nabla}{k^2} \right] g(\mathbf{r},\mathbf{r}') = \left[I + \frac{\nabla\nabla}{k^2} \right] \frac{e^{ikr}}{r}. \tag{18}$$

It can be seen from the last expression in equation (18) that $g(\boldsymbol{r},\boldsymbol{r}')$ is only dependent on the distance between observation and source point and thus can be replaced by $g(|\boldsymbol{r}-\boldsymbol{r}'|)$. Correspondingly, we apply the impedance operator that only regards the direct field interaction to an arbitrary current distribution that is operated on by a transformation operator P_R,

$$\int_V \overline{G}_0(\mathbf{r},\mathbf{r}') \cdot P_R \mathbf{J}(\mathbf{r}')\, dv' = \int_V \left[I + \frac{\nabla\nabla}{k^2} \right] g\left(|\mathbf{r}-\mathbf{r}'|\right) \cdot R \cdot \mathbf{J}\left(R^{-1}\mathbf{r}'\right) dv'. \tag{19}$$

To tackle equation (19), we perform a change of variables to the original source coordinate system, i.e. $\mathbf{x}' = R^{-1}\boldsymbol{r}'$,

$$\begin{aligned} \int_V \left[I + \frac{\nabla\nabla}{k^2} \right] g\left(|\mathbf{r}-R\mathbf{x}'|\right) \cdot R \cdot \mathbf{J}(\mathbf{x}') \left|\det(R)\right| d\tau' &= \int_V \left[I + \frac{\nabla\nabla}{k^2} \right] g\left(|\mathbf{r}-R\mathbf{x}'|\right) \cdot R \cdot \mathbf{J}(\mathbf{x}')\, d\tau' \\ &= \int_V \left[I + \frac{\nabla\nabla}{k^2} \right] g\left(\left|R^{-1}\mathbf{r}-\mathbf{x}'\right|\right) \cdot R \cdot \mathbf{J}(\mathbf{x}')\, d\tau' \end{aligned} \tag{20}$$

In the above derivation, we use the following facts:

1) Since we have changed variables, a Jacobian must appear in combination with the infinitesimal element, that is, $dv' = |det(R)| \cdot d\tau'$. However, the symmetry operation R is represented by an orthogonal matrix. Since the absolute value of the determinant of an orthogonal matrix is 1, this term is dropped in the second expression.
2) The integral limits in equation (20) are unchanged only because we assume that the structure is invariant under the symmetry operation R.
3) To reach the last expression, we notice that any orthogonal transformation does not affect the distance between two points.

Notice that the gradient operator in equation (20) is taken with respect to the original observation coordinate system. In the transformed coordinate, the gradient operator reads,

$$\begin{aligned} \nabla \cdot \mathbf{f}\left(R^{-1}\mathbf{r}\right) &= \frac{\partial}{\partial x} f_x\left(R^{-1}\mathbf{r}\right) + \frac{\partial}{\partial y} f_y\left(R^{-1}\mathbf{r}\right) + \frac{\partial}{\partial z} f_z\left(R^{-1}\mathbf{r}\right) \\ &= \frac{\partial}{\partial X} f_x(\mathbf{x}) \frac{\partial X}{\partial x} + \frac{\partial}{\partial Y} f_x(\mathbf{x}) \frac{\partial Y}{\partial x} + \frac{\partial}{\partial Z} f_x(\mathbf{x}) \frac{\partial Z}{\partial x} \\ &\quad + \frac{\partial}{\partial X} f_y(\mathbf{x}) \frac{\partial X}{\partial y} + \frac{\partial}{\partial Y} f_y(\mathbf{x}) \frac{\partial Y}{\partial y} + \frac{\partial}{\partial Z} f_y(\mathbf{x}) \frac{\partial Z}{\partial y} \\ &\quad + \frac{\partial}{\partial X} f_z(\mathbf{x}) \frac{\partial X}{\partial z} + \frac{\partial}{\partial Y} f_z(\mathbf{x}) \frac{\partial Y}{\partial z} + \frac{\partial}{\partial Z} f_z(\mathbf{x}) \frac{\partial Z}{\partial z} \\ &= \nabla_{\mathbf{x}} \cdot R^{-1} \cdot \mathbf{f}(\mathbf{x}). \end{aligned} \tag{21}$$

$$\nabla f\left(R^{-1}\mathbf{r}\right)=\begin{pmatrix}\frac{\partial}{\partial x}f\left(\mathbf{x}\right)\\ \frac{\partial}{\partial y}f\left(\mathbf{x}\right)\\ \frac{\partial}{\partial z}f\left(\mathbf{x}\right)\end{pmatrix}=\begin{pmatrix}\frac{\partial X}{\partial x} & \frac{\partial Y}{\partial x} & \frac{\partial Z}{\partial x}\\ \frac{\partial X}{\partial y} & \frac{\partial Y}{\partial y} & \frac{\partial Z}{\partial y}\\ \frac{\partial X}{\partial z} & \frac{\partial Y}{\partial z} & \frac{\partial Z}{\partial z}\end{pmatrix}\begin{pmatrix}\frac{\partial}{\partial X}f\left(\mathbf{x}\right)\\ \frac{\partial}{\partial Y}f\left(\mathbf{x}\right)\\ \frac{\partial}{\partial Z}f\left(\mathbf{x}\right)\end{pmatrix}=R\cdot\nabla_{\mathbf{x}}f\left(\mathbf{x}\right). \tag{22}$$

Combining equation (21) and equation (22) with equation (20), the last expression in equation (20) becomes

$$R\cdot\int_V\left[I+\frac{\nabla_{\mathbf{x}}\nabla_{\mathbf{x}}}{k^2}\right]g\left(\left|R^{-1}\mathbf{r}-\mathbf{x}'\right|\right)\cdot\mathbf{J}\left(\mathbf{x}'\right)d\tau'=R\cdot\int_V\overline{G}_0\left(R^{-1}\mathbf{r},\mathbf{x}'\right)\cdot\mathbf{J}\left(\mathbf{x}'\right)d\tau'. \tag{23}$$

In the derivation of equation (23), it is noticed that I is simply an identity operator. As a result, the commutative relation between the direct wave impedance part and the transformation operator is proved,

$$\int_V\overline{G}_0\left(\mathbf{r},\mathbf{r}'\right)\cdot P_R\mathbf{J}\left(\mathbf{r}'\right)dv'=P_R\int_V\overline{G}_0\left(\mathbf{r},\mathbf{r}'\right)\cdot\mathbf{J}\left(\mathbf{r}'\right)dv'. \tag{24}$$

For the reflected wave part, we can express its corresponding Green's function in the Cartesian coordinate system as well as in the cylindrical coordinate system, that is,

$$\overline{G}_r^{s/p}\left(\mathbf{r},\mathbf{r}'\right)=\overline{G}_r^{s/p}\left(\varphi,\rho,z+z'\right). \tag{25}$$

In equation (25), it is emphasized that the reflected wave is dependent on a relative angle φ, a transverse distance ρ and the sum of vertical distances $z+z'$ between the observation point and the source point,

$$\tan\left(\varphi\right)=\frac{y-y'}{x-x'},\ \rho=\sqrt{\left(x-x'\right)^2+\left(y-y'\right)^2}. \tag{26}$$

The superscript in equation (25) refers to the *s*-polarized and the *p*-polarized parts for the reflected wave. A closed form expression in the spatial domain reads,

$$\begin{aligned}\overline{G}_{r,\|}^{s}\left(\mathbf{r},\mathbf{r}'\right)&=\overline{G}_{r,\|}^{s}\left(\varphi,\rho,z+z'\right)\\&=\frac{i}{4}\begin{pmatrix}\cos 2\varphi & \sin 2\varphi\\ \sin 2\varphi & -\cos 2\varphi\end{pmatrix}F_1^s\left(\rho,z+z'\right)+\frac{i}{4}\begin{pmatrix}1 & 0\\ 0 & 1\end{pmatrix}F_2^s\left(\rho,z+z'\right),\end{aligned} \tag{27}$$

$$\begin{aligned}\overline{G}_{r,\|}^{p}\left(\mathbf{r},\mathbf{r}'\right)&=\overline{G}_{r,\|}^{p}\left(\varphi,\rho,z+z'\right)\\&=\frac{i}{4}\begin{pmatrix}\cos 2\varphi & \sin 2\varphi\\ \sin 2\varphi & -\cos 2\varphi\end{pmatrix}F_1^p\left(\rho,z+z'\right)-\frac{i}{4}\begin{pmatrix}1 & 0\\ 0 & 1\end{pmatrix}F_2^p\left(\rho,z+z'\right).\end{aligned} \tag{28}$$

In equation (27) and (28), the functions F_1^s, F_2^s, F_1^p *and* F_2^p are only dependent on the transverse and vertical distances and the detailed functional form of these functions are not of interest in this work. Note that equation (27) and (28) ignore the horizontal – vertical, vertical – horizontal, and vertical – vertical couplings, since they are not affected by the symmetry operations given in equation (15).

Next, we apply the reflected wave Green's function to an operated current,

$$\int_V \overline{G}_r^{s/p}\left(\mathbf{r},\mathbf{r}'\right)\cdot P_R\mathbf{J}\left(\mathbf{r}'\right)dv' = \int_V \overline{G}_r^{s/p}\left(R\mathbf{x},R\mathbf{x}'\right)\cdot R\cdot\mathbf{J}\left(\mathbf{x}'\right)dv'. \tag{29}$$

In equation (29) the same change of variables as in equation (20) is employed. To find a relation between the original and transformed coordinate system, it is noticed that the rotated source coordinate $\mathbf{x}'$ and the rotated observation coordinate $\mathbf{x}$ have no effect on the vertical distance $z + z'$ and the transverse distance ρ, that is, $\rho(\boldsymbol{r},\boldsymbol{r}') = \rho(\boldsymbol{x},\boldsymbol{x}')$. However, the relative angle φ is altered,

$$\varphi = \theta + \varphi' \text{ for rotations,} \tag{30}$$

$$\varphi = 2\theta - \varphi' \text{ for reflections.} \tag{31}$$

Combining the above observations and applying to the relative angle, the transverse distance and the vertical distance, we can re-write equation (27) and equation (28). Take equation (27) as an example,

$$\begin{aligned}\overline{G}_{r,\parallel}^{s}\left(R\mathbf{x},R\mathbf{x}'\right) &= \overline{G}_{r,\parallel}^{s}\left(\theta+\varphi',\rho,z+z'\right)\\ &= \frac{i}{4}\begin{pmatrix}\cos 2\left(\theta+\varphi'\right) & \sin 2\left(\theta+\varphi'\right)\\ \sin 2\left(\theta+\varphi'\right) & -\cos 2\left(\theta+\varphi'\right)\end{pmatrix}F_1^s\left(\rho,z+z'\right)+\frac{i}{4}\begin{pmatrix}1 & 0\\ 0 & 1\end{pmatrix}F_2^s\left(\rho,z+z'\right),\end{aligned} \tag{32}$$

$$\begin{aligned}\overline{G}_{r,\parallel}^{s}\left(R\mathbf{x},R\mathbf{x}'\right) &= \overline{G}_{r,\parallel}^{s}\left(2\theta-\varphi',\rho,z+z'\right)\\ &= \frac{i}{4}\begin{pmatrix}\cos 2\left(2\theta-\varphi'\right) & \sin 2\left(2\theta-\varphi'\right)\\ \sin 2\left(2\theta-\varphi'\right) & -\cos 2\left(2\theta-\varphi'\right)\end{pmatrix}F_1^s\left(\rho,z+z'\right)+\frac{i}{4}\begin{pmatrix}1 & 0\\ 0 & 1\end{pmatrix}F_2^s\left(\rho,z+z'\right).\end{aligned} \tag{33}$$

equation (32) and (33) are respectively for rotation and reflection operations. As suggested by equation (29), we right-multiply equation (32) and (33) by R. It can be proven that

$$\begin{pmatrix}\cos 2\left(\theta+\varphi'\right) & \sin 2\left(\theta+\varphi'\right)\\ \sin 2\left(\theta+\varphi'\right) & -\cos 2\left(\theta+\varphi'\right)\end{pmatrix}\begin{pmatrix}\cos\theta & -\sin\theta\\ \sin\theta & \cos\theta\end{pmatrix}=\begin{pmatrix}\cos\theta & -\sin\theta\\ \sin\theta & \cos\theta\end{pmatrix}\begin{pmatrix}\cos 2\varphi' & \sin 2\varphi'\\ \sin 2\varphi' & -\cos 2\varphi'\end{pmatrix}. \tag{34}$$

$$\begin{pmatrix}\cos 2\left(2\theta-\varphi'\right) & \sin 2\left(2\theta-\varphi'\right)\\ \sin 2\left(2\theta-\varphi'\right) & -\cos 2\left(2\theta-\varphi'\right)\end{pmatrix}\begin{pmatrix}\cos 2\theta & \sin 2\theta\\ \sin 2\theta & -\cos 2\theta\end{pmatrix}=\begin{pmatrix}\cos 2\theta & \sin 2\theta\\ \sin 2\theta & -\cos 2\theta\end{pmatrix}\begin{pmatrix}\cos 2\varphi' & \sin 2\varphi'\\ \sin 2\varphi' & -\cos 2\varphi'\end{pmatrix}. \tag{35}$$

Subsequently, we have

$$\overline{G}_{r,\parallel}^{s}\left(R\mathbf{x},R\mathbf{x}'\right)\cdot R = R\cdot\overline{G}_{r,\parallel}^{s}\left(\mathbf{x},\mathbf{x}'\right). \tag{36}$$

Similar proofs can be constructed for the *p*-polarized light as well. Substituting equation (36) into equation (29) immediately gives,

$$\int_V \overline{G}_r^{s/p}\left(\mathbf{r},\mathbf{r}'\right)\cdot P_R\mathbf{J}\left(\mathbf{r}'\right)dv' = R\cdot\int_V \overline{G}_r^{s/p}\left(\mathbf{x},\mathbf{x}'\right)\cdot\mathbf{J}\left(\mathbf{x}'\right)dv' = P_R\int_V \overline{G}_r^{s/p}\left(\mathbf{r},\mathbf{r}'\right)\cdot\mathbf{J}\left(\mathbf{r}'\right)dv'. \qquad (37)$$

Hence, the commutative relation between the dyadic Green's function used in this work and the rotation and reflection symmetry operations is proved.

Supplementary Discussion 4: On the Symmetry of the Square Structures

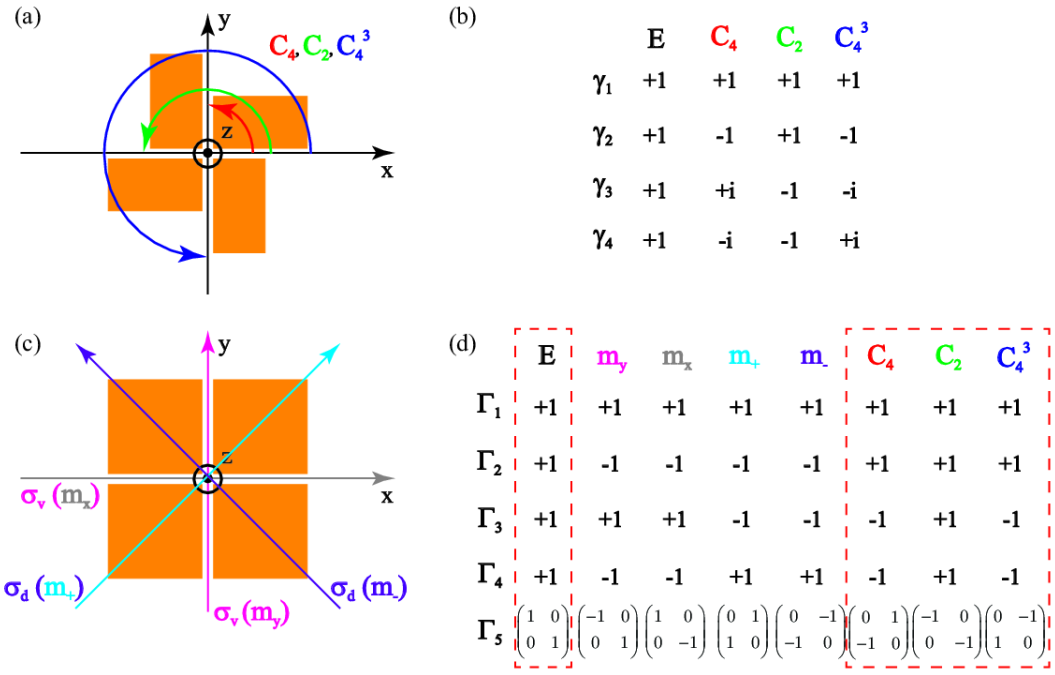

	E	C_4	C_2	C_4^3
γ_1	+1	+1	+1	+1
γ_2	+1	-1	+1	-1
γ_3	+1	+i	-1	-i
γ_4	+1	-i	-1	+i

	E	m_y	m_x	m_+	m_-	C_4	C_2	C_4^3
Γ_1	+1	+1	+1	+1	+1	+1	+1	+1
Γ_2	+1	-1	-1	-1	-1	+1	+1	+1
Γ_3	+1	+1	+1	-1	-1	-1	+1	-1
Γ_4	+1	-1	-1	+1	+1	-1	+1	-1
Γ_5	$\begin{pmatrix}1&0\\0&1\end{pmatrix}$	$\begin{pmatrix}-1&0\\0&1\end{pmatrix}$	$\begin{pmatrix}1&0\\0&-1\end{pmatrix}$	$\begin{pmatrix}0&1\\1&0\end{pmatrix}$	$\begin{pmatrix}0&-1\\-1&0\end{pmatrix}$	$\begin{pmatrix}0&1\\-1&0\end{pmatrix}$	$\begin{pmatrix}-1&0\\0&-1\end{pmatrix}$	$\begin{pmatrix}0&-1\\1&0\end{pmatrix}$

Supplementary Figure 10 Illustration of symmetry operations in the C_4 group (**a**) and the C_{4v} group (**c**) and the groups' character tables (**b** and **d**).

By comparing **Supplementary Figure 10** (a) with (c) and Supplementary Figure 10 (b) with (d), we can readily see that the C_{4v} group actually includes all the symmetry operations that are in the C_4 group. Therefore, an irreducible representation of the C_{4v} group is still a representation of the C_4 group if only the identity operation and the rotation operations $C_4, C_2, and\ C_4^3$ are considered. But this representation is in general a reducible representation of the C_4 group. The fact that the C_4 group has a lower symmetry may indicate that the 2-fold degeneracy suggested by the C_{4v} group may be lifted. How this degeneracy is lifted can be answered by checking how many times the irreducible representations of the C_4 group is included in a reducible representation.

Mathematically, the number of times can be calculated by referring to the characters [3],

$$a_{(j)}^{(i)} = \frac{1}{h}\sum_{R} \chi_{G'}^{(j)}(R)^{*}\, \chi_{G}^{(i)}(R). \tag{38}$$

In equation (38), a represents the number of times the j^{th} irreducible representation of the G' group appearing in the i^{th} reducible representation of the G group. In the current scenario, the G' group and the G group are the C_4 group and the C_{4v} group. Furthermore, the sum is taken over all the symmetry operations (in total h) in the G' group. χ is the character of a representation and is defined as the sum of the diagonal elements of a representation.

In the following, we find that how many times $\gamma_1, \gamma_2, \gamma_3, and\ \gamma_4$ (the irreducible representations of the C_4 group) are included in $\Gamma_1, \Gamma_2, \Gamma_3, \Gamma_4\ and\ \Gamma_5$ (the irreducible

representations of the C_{4v} group) respectively. Since Γ_1 and Γ_2 have the same representation for the identity and the rotation operations, they can be treated together,

$$\begin{aligned}
a_{\gamma_1}^{\Gamma_1/\Gamma_2} &= \frac{1}{4}\left[(+1)\cdot(+1)+(+1)\cdot(+1)+(+1)\cdot(+1)+(+1)\cdot(+1)\right]=1,\\
a_{\gamma_2}^{\Gamma_1/\Gamma_2} &= \frac{1}{4}\left[(+1)\cdot(+1)+(-1)\cdot(+1)+(+1)\cdot(+1)+(-1)\cdot(+1)\right]=0,\\
a_{\gamma_3}^{\Gamma_1/\Gamma_2} &= \frac{1}{4}\left[(+1)\cdot(+1)+(-i)\cdot(+1)+(-1)\cdot(+1)+(+i)\cdot(+1)\right]=0,\\
a_{\gamma_4}^{\Gamma_1/\Gamma_2} &= \frac{1}{4}\left[(+1)\cdot(+1)+(+i)\cdot(+1)+(-1)\cdot(+1)+(-i)\cdot(+1)\right]=0.
\end{aligned} \tag{39}$$

For Γ_3 and Γ_4, we obtain

$$\begin{aligned}
a_{\gamma_1}^{\Gamma_3/\Gamma_4} &= \frac{1}{4}\left[(+1)\cdot(+1)+(+1)\cdot(-1)+(+1)\cdot(+1)+(+1)\cdot(-1)\right]=0,\\
a_{\gamma_2}^{\Gamma_3/\Gamma_4} &= \frac{1}{4}\left[(+1)\cdot(+1)+(-1)\cdot(-1)+(+1)\cdot(+1)+(-1)\cdot(-1)\right]=1,\\
a_{\gamma_3}^{\Gamma_3/\Gamma_4} &= \frac{1}{4}\left[(+1)\cdot(+1)+(-i)\cdot(-1)+(-1)\cdot(+1)+(+i)\cdot(-1)\right]=0,\\
a_{\gamma_3}^{\Gamma_3/\Gamma_4} &= \frac{1}{4}\left[(+1)\cdot(+1)+(+i)\cdot(-1)+(-1)\cdot(+1)+(-i)\cdot(-1)\right]=0.
\end{aligned} \tag{40}$$

For Γ_5, we have

$$\begin{aligned}
a_{\gamma_1}^{\Gamma_5} &= \frac{1}{4}\left[(+1)\cdot(+2)+(+1)\cdot(0)+(+1)\cdot(-2)+(+1)\cdot(0)\right]=0,\\
a_{\gamma_2}^{\Gamma_5} &= \frac{1}{4}\left[(+1)\cdot(+2)+(-1)\cdot(0)+(+1)\cdot(-2)+(-1)\cdot(0)\right]=0,\\
a_{\gamma_3}^{\Gamma_5} &= \frac{1}{4}\left[(+1)\cdot(+2)+(-i)\cdot(0)+(-1)\cdot(-2)+(+i)\cdot(0)\right]=1,\\
a_{\gamma_4}^{\Gamma_5} &= \frac{1}{4}\left[(+1)\cdot(+2)+(+i)\cdot(0)+(-1)\cdot(-2)+(-i)\cdot(0)\right]=1.
\end{aligned} \tag{41}$$

Based on the above equations, when all the mirroring symmetries are removed, Γ_1/Γ_2 of the C_{4v} group will become the first irreducible representation γ_1 of the C_4 group. Similarly, Γ_3/Γ_4 of the C_{4v} group will form the irreducible representation γ_2 of the C_4 group. Lastly, the 2-dimensional irreducible representation Γ_5 of the C_{4v} group breaks into the irreducible representations γ_3 *and* γ_4 of the C_4 group. In this way, we can properly link the eigenmodes associated with different irreducible representations of the C_4 group with the eigenmodes associated with different irreducible representations of the C_{4v} group.

It is known that a projection operator can be defined for the I^{th} irreducible representation of a group G[3],

$$\mathcal{P}_G^{(i)} = \frac{l_G^{(i)}}{h_G}\sum_R \chi_G^{(i)}\left(R\right)^* P_R. \tag{42}$$

In equation (42), $l_G^{(i)}$ *and* h_G are the dimensionality of the i^{th} irreducible representation of a group G and the number of elements in the group. $\chi_G^{(i)}(R)$ and P_R are the character of the i^{th} irreducible representation and the transformation operator for a symmetry operation in the group. Lastly, the summation is conducted with respect to all the symmetry operations in the group. Following Wigner's convention [3], the transformation operator is defined as,

$$P_R f\left(\mathbf{x}\right) = f\left(R^{-1}\mathbf{x}\right),\ P_R \mathbf{f}\left(\mathbf{x}\right) = R \cdot \mathbf{f}\left(R^{-1}\mathbf{x}\right). \tag{43}$$

In equation (43), the first equation and the second equation are for scalar and vector functions, respectively. Here, we especially focus on the 5th irreducible representation of the C_{4v} group. equation (42) reads,

$$\mathcal{P}_{C_{4v}}^{\Gamma_5} = \frac{1}{4}\left(\chi_{C_{4v}}^{\Gamma_5}\left(E\right)^* \cdot P_E + \chi_{C_{4v}}^{\Gamma_5}\left(C_4\right)^* \cdot P_{C_4} + \chi_{C_{4v}}^{\Gamma_5}\left(C_2\right)^* \cdot P_{C_2} + \chi_{C_{4v}}^{\Gamma_5}\left(C_4^3\right)^* \cdot P_{C_4^3}\right). \tag{44}$$

In equation (44) the mirroring operations are omitted because 1) they are not the elements that are shared by the C_{4v} group and the C_4 group; 2) their characters are zero. Further, we notice that the characters of the 5th irreducible representation of the C_{4v} group can be expressed in terms of the characters of the irreducible representations of the C_4 group [3],

$$\chi_{C_{4v}}^{\Gamma_5}\left(R\right) = a_{\gamma_1}^{\Gamma_5} \cdot \chi_{C_4}^{\gamma_1}\left(R\right) + a_{\gamma_2}^{\Gamma_5} \cdot \chi_{C_4}^{\gamma_2}\left(R\right) + a_{\gamma_3}^{\Gamma_5} \cdot \chi_{C_4}^{\gamma_3}\left(R\right) + a_{\gamma_4}^{\Gamma_5} \cdot \chi_{C_4}^{\gamma_4}\left(R\right). \tag{45}$$

Substituting equation (45) into equation (44), we recollect all the terms according to the irreducible representations,

$$\begin{aligned}\mathcal{P}_{C_{4v}}^{\Gamma_5} &= \frac{1}{4}\left(a_{\gamma_1}^{\Gamma_5} \cdot \sum_R \chi_{C_4}^{\gamma_1}\left(R\right)^* P_R + a_{\gamma_2}^{\Gamma_5} \cdot \sum_R \chi_{C_4}^{\gamma_2}\left(R\right)^* P_R + a_{\gamma_3}^{\Gamma_5} \cdot \sum_R \chi_{C_4}^{\gamma_3}\left(R\right)^* P_R + a_{\gamma_4}^{\Gamma_5} \cdot \sum_R \chi_{C_4}^{\gamma_4}\left(R\right)^* P_R\right) \\ &= a_{\gamma_1}^{\Gamma_5} \cdot \mathcal{P}_{C_4}^{(1)} + a_{\gamma_2}^{\Gamma_5} \cdot \mathcal{P}_{C_4}^{(2)} + a_{\gamma_3}^{\Gamma_5} \cdot \mathcal{P}_{C_4}^{(3)} + a_{\gamma_4}^{\Gamma_5} \cdot \mathcal{P}_{C_4}^{(4)}.\end{aligned} \tag{46}$$

In the derivation of the last equation in equation (46), the definition for the projection operation in equation (42) is reused. By noticing the results from the above, we can conclude that

$$\mathcal{P}_{C_{4v}}^{(5)} = \mathcal{P}_{C_4}^{(3)} + \mathcal{P}_{C_4}^{(4)}. \tag{47}$$

Since 1) the application of the projection operator $\mathcal{P}_{C_{4v}}^{(5)}$ on the left hand side of equation (47) to all the eigenmodes of the four square structure actually give the modes that belong to the 5th irreducible representation and 2) the projection operator $\mathcal{P}_{C_{4v}}^{(5)}$ is the sum of two operators that

are associated with the 3rd and 4th irreducible representations of the four bar structure, the projected eigenmodes should be a mix of the eigenmodes that belong to the 3rd and 4th irreducible representations of the four bar structure. Consequently, the excitation of a mode in the four square structure by a circularly polarized light will introduce the response from both the “left” mode and the “right” mode.

References

1. Zheng, X. *et al.* Volumetric method of moments and conceptual multilevel building blocks for nanotopologies. *IEEE Photonics J.* **4,** 267–282 (2012).
2. Zheng, X. *et al.* On the Use of Group Theory in Understanding the Optical Response of a Nanoantenna. *IEEE Trans. Antennas Propag.* **63,** 1589–1602 (2015).
3. Tinkham, M. *Group Theory and Quantum Mechanics*. (Dover Publications, 2003).
4. Wigner, E. P. & Griffin, J. J. *Group Theory and Its Application to the Quantum Mechanics of Atomic Spectra*. (Academic Press, 1959).